

Star formation towards the Galactic H II region RCW 120

Herschel★ observations of compact sources

M. Figueira¹, A. Zavagno¹, L. Deharveng¹, D. Russeil¹, L.D. Anderson², A. Men'shchikov³, N. Schneider⁴, T. Hill¹, F. Motte^{5,3}, P. Mège¹, G. LeLeu¹, H. Roussel⁶, J.-P. Bernard^{7,8}, A. Traficante⁹, D. Paradis^{7,8}, J. Tigé¹, P. André³, S. Bontemps¹⁰, and A. Abergel¹¹

¹ Aix Marseille Univ, CNRS, LAM, Laboratoire d'Astrophysique de Marseille, Marseille, France

² West Virginia University, Department of Physics & Astronomy, Morgantown, WV 26506, USA

³ Laboratoire AIM Paris-Saclay, CEA/IRFU - CNRS/INSU - Université Paris Diderot, Service d'Astrophysique, Bât. 709, CEA-Saclay, 91191 Gif-sur-Yvette CEDEX, France

⁴ Physik. Institut, University of Cologne, Zùlpicher Str. 77, 50937, Koeln, Germany

⁵ Institut de Planétologie et d'Astrophysique de Grenoble (IPAG), Univ. Grenoble Alpes / CNRS-INSU, BP 53, 38041 Grenoble Cedex 9, France

⁶ Institut d'Astrophysique de Paris, UMR 7095 CNRS, Université Pierre & Marie Curie, 98 bis Boulevard Arago, 75014 Paris, France

⁷ CNRS, IRAP, 9 Av. colonel Roche, BP 44346, F-31028 Toulouse cedex 4, France

⁸ Université de Toulouse, UPS-OMP, IRAP, F-31028 Toulouse cedex 4, France

⁹ Istituto Nazionale di Astrofisica - IAPS, Via Fosso del Cavaliere 100, I-00133 Roma, Italy

¹⁰ CNRS/INSU, Laboratoire d'Astrophysique de Bordeaux, UMR 5804, BP 89, 33271, Floirac CEDEX, France

¹¹ Institut d'Astrophysique Spatiale, UMR 8617, CNRS, Université Paris-Sud 11, 91405, Orsay, France

Received July 22 2016; accepted December 1 2016

ABSTRACT

Context. The expansion of H II regions can trigger the formation of stars. An overdensity of young stellar objects (YSOs) is observed at the edges of H II regions but the mechanisms that give rise to this phenomenon are not clearly identified. Moreover, it is difficult to establish a causal link between H II-region expansion and the star formation observed at the edges of these regions. A clear age gradient observed in the spatial distribution of young sources in the surrounding might be a strong argument in favor of triggering.

Aims. We aim to characterize the star formation observed at the edges of H II regions by studying the properties of young stars that form there. We aim to detect young sources, derive their properties and their evolution stage in order to discuss the possible causal link between the first-generation massive stars that form the H II region and the young sources observed at their edges.

Methods. We have observed the Galactic H II region RCW 120 with *Herschel* PACS and SPIRE photometers at 70, 100, 160, 250, 350 and 500 μm . We produced temperature and H₂ column density maps and use the *getsources* algorithm to detect compact sources and measure their fluxes at *Herschel* wavelengths. We have complemented these fluxes with existing infrared data. Fitting their spectral energy distributions (SEDs) with a modified blackbody model, we derived their envelope dust temperature and envelope mass. We computed their bolometric luminosities and discuss their evolutionary stages.

Results. The overall temperatures of the region (without background subtraction) range from 15 K to 24 K. The warmest regions are observed towards the ionized gas. The coldest regions are observed outside the ionized gas and follow the emission of the cold material previously detected at 870 μm and 1.3 mm. The H₂ column density map reveals the distribution of the cold medium to be organized in filaments and highly structured. Column densities range from $7 \times 10^{21} \text{ cm}^{-2}$ up to $9 \times 10^{23} \text{ cm}^{-2}$ without background subtraction. The cold regions observed outside the ionized gas are the densest and host star formation when the column density exceeds $2 \times 10^{22} \text{ cm}^{-2}$. The most reliable 35 compact sources are discussed. Using existing CO data and morphological arguments we show that these sources are likely to be associated with the RCW 120 region. These sources' volume densities range from $2 \times 10^5 \text{ cm}^{-3}$ to 10^8 cm^{-3} . Five sources have envelope masses larger than $50 M_{\odot}$ and are all observed in high column density regions ($> 7 \times 10^{22} \text{ cm}^{-2}$). We find that the evolutionary stage of the sources primarily depends on the density of their hosting condensation and is not correlated with the distance to the ionizing star.

Conclusions. The *Herschel* data, with their unique sampling of the far infrared domain, have allowed us to characterize the properties of compact sources observed towards RCW 120 for the first time. We have also been able to determine the envelope temperature, envelope mass and evolutionary stage of these sources. Using these properties we have shown that the density of the condensations that host star formation is a key parameter of the star-formation history, irrespective of their projected distance to the ionizing stars.

Key words. ISM: H II regions – Stars: formation – ISM: individual objects: RCW 120

1. Introduction

Massive stars ($M > 8 M_{\odot}$) affect their surrounding medium due to the action of both their ionizing photons and stellar winds. They

Send offprint requests to: M. Figueira, miguel.figueira@lam.fr

* *Herschel* is an ESA space observatory with science instruments provided by European-led Principal Investigator consortia and with important participation from NASA.

form ionized ($H\text{II}$) regions that expand, bordered by a shell of swept-up neutral material (Dyson & Williams 1997). Star formation is observed at the edges of Galactic and extragalactic $H\text{II}$ regions (Bernard et al. 2016). Young stars form there either spontaneously or through various mechanisms linked to the expansion of the ionized region (Deharveng et al. 2010).

Star formation observed at the edges of $H\text{II}$ regions has been studied in detail during the past ten years. With the GLIMPSE (Benjamin et al. 2003) and MIPS GAL (Carey et al. 2009) surveys, the *Spitzer* satellite has revealed that we live in a bubbling galactic disk where thousands of $H\text{II}$ regions have a clear impact on their environment. Anderson et al. (2011) have shown that half of all $H\text{II}$ regions have a bubble morphology. Studies of triggering have focused on bubble $H\text{II}$ regions. Deharveng et al. (2010) used *Spitzer* GLIMPSE and MIPS GAL data combined with ATLAS GAL (Schuller et al. 2009) data on 102 bubbles. They showed that star formation observed at the edges of $H\text{II}$ regions is an important phenomenon in our Galaxy. Up to 25% of the ionized regions show high-mass star formation triggered on their edges. This result has been confirmed by Thompson et al. (2012) and Kendrew et al. (2012, 2016) who found an overdensity of young stellar objects (YSOs), including massive objects, around *Spitzer* and ATLAS GAL bubbles. Simpson et al. (2012) have listed 5106 bubbles using these GLIMPSE and MIPS GAL surveys. Many studies of individual $H\text{II}$ regions, including numerical simulations, confirm that $H\text{II}$ regions impact on their surrounding, enhancing significantly the star formation there (Minier et al. 2013; Samal et al. 2014; Liu et al. 2015; Ladeyschikov et al. 2015). This impact is also observed at the waist of bipolar $H\text{II}$ regions as recently discovered by Deharveng et al. (2015).

However Dale et al. (2015) assessed the relevance of standard observational criteria used to decide whether the star-formation process is of spontaneous or triggered origin at the edges of $H\text{II}$ region. By comparing the observational criteria used to their own new numerical results they concluded that, when interpreting observations of star formation in the vicinity of feedback-driven structures in terms of triggering, one should exercise caution.

While the large and rapidly increasing bulk of knowledge tends to offer empirical evidence in support of some impact of $H\text{II}$ regions on the local star formation, there are still many unanswered questions on the possible influence of these regions on star formation near their edges. One way to firmly establish the causal link existing between the ionized region and the star-formation process taking place on its surrounding could be to measure a clear difference between the age of the ionizing stars, located in the central $H\text{II}$ region and the ones formed at its edges (Martins et al. 2010; Bik et al. 2010). However, the determination of stellar ages is challenging (Martins et al. 2010).

We are left in a situation where we observe an overdensity of young stars at the edges of these $H\text{II}$ regions. These young stars are highly efficient (up to 25%) at forming massive stars. (Bik et al. 2010; Ellerbroek et al. 2013; Cappa et al. 2014; Tapia et al. 2014). But we do not know how the material is assembled (uniformly distributed then collected versus pre-condensed in an inhomogeneous medium) and what are the mechanisms that control the formation of stars in these regions. For pre-existing clumps, star formation could occur spontaneously before encountering the ionization front or the ionizing radiation leaking from the $H\text{II}$ region. Dedicated observations can help in answering these questions. High resolution molecular spectroscopy reveals the distribution and velocity field of the material that surrounds $H\text{II}$ regions (Anderson et al. 2015a; Liu et al. 2015). The

spatial distribution, properties and evolutionary stage of YSOs are key points to address the triggering issue. We need to obtain an overview of all stages of star formation in a given region and access the distribution of the surrounding material on all spatial scales to discuss the history of star formation. The large scale distribution should help in understanding the initial distribution of the material (uniform versus clumpy, filamentary). A better knowledge of the distribution and properties (density, temperature) of the material that surrounds $H\text{II}$ regions could also help in better understanding how the material is assembled and how star formation occurs around ionized regions.

The *Herschel* satellite offers a unique opportunity to study star formation around Galactic $H\text{II}$ regions and helps in answering some of the pending questions. Thanks to its sensitivity and its large wavelength coverage in the far-infrared, *Herschel* is perfectly suited to study the earliest phases of star formation. The six measured photometric points (70, 100, 160, 250, 350, 500 μm) really help in constraining the young sources' properties (temperature, envelope mass, luminosity). Moreover, *Herschel*'s wavelength range covers the peak of the YSOs' spectral energy distribution (SED) also helping to characterize the young source' evolutionary stage. Combined with existing infrared and molecular data, *Herschel* observations allow us to obtain a global view of the star-formation history (Nguyen et al. 2015).

Here we present the results obtained for young compact sources observed towards the bubble $H\text{II}$ region RCW 120. Using *Herschel* photometric PACS and SPIRE data, we re-examine this region to better determine the nature and evolutionary stage of the YSOs observed there. We aim to discuss the region's star-formation history there using sources' evolutionary stage. Section 2 presents the current knowledge on RCW 120. The *Herschel* observations are described in Sect. 3. The data reduction and sources' extraction are presented in Sect. 4. The results are presented in Sect. 5 and discussed in Sect. 6. The main results and conclusions are given in Sect. 7.

2. The RCW 120 region

RCW 120 (Rodgers et al. 1960) is an egg-shaped Galactic $H\text{II}$ region of 3.8 pc diameter, located 0.5° above the Galactic plane. Due to its simple morphology and isolation, this region has been studied in detail during the past ten years. The main results are summarized below:

The region is ionized by an O8V star, CD-38 $^\circ$ 11636 (Zavagno et al. 2007, hereafter ZAV07; Martins et al. 2010). An emission arc is observed at 24 μm below the star (Deharveng et al. 2009, hereafter DEH09; Martins et al. 2010, see their fig. 3) and is interpreted as representing the upstream boundary between the wind bubble and the photoionized interstellar medium (Mackey et al. 2015).

The photometric distance of RCW 120 was computed by Russeil (2003) using UBV and $H\beta$ photometry. The uncertainty is estimated to be 0.6 kpc and comes from the uncertainty in the spectral type estimate (around 0.3 mag).

RCW 120 and its surrounding layer have been observed in the dust continuum at 870 μm (DEH09) and 1.3 mm (ZAV07) and in CO molecular lines (Anderson et al. 2015a; Torii et al. 2015). These observations show that RCW 120 is surrounded by a dense shell of gas and dust.

Torii et al. (2015) observed two molecular clouds towards RCW 120 and suggest that some collision between the clouds triggered the formation of the ionizing O star of RCW 120 in a

short timescale of 0.2-0.4 Myr. An age of 0.4 Myr is also obtained by Mackey et al. (2015). Simulations from Tremblin et al. (2014a) lead to a similar age for the ionizing star of RCW 120.

Anderson et al. (2015a) found no evidence for expansion of the molecular material associated with RCW 120 and therefore can make no claim about its geometry (2D or 3D). Dust emission simulations suggest that the H II region RCW 120 is not spherical, but instead cylindrical, and that we observe the object along the axis of this cylinder (Pavlyuchenkov et al. 2013).

Using 1.3 mm continuum emission ZAV07 found eight condensations (five located at the edges of the ionized region, see their Fig. 4) and studied the young stellar content of these condensations, pointing out the possible importance of long-distance influence of the ionized region on its surrounding. This study has been completed by DEH09 who characterized the evolutionary stage by adding $24\ \mu\text{m}$ data from MIPS GAL and confirmed the importance of long-distance interaction between the H II region and its surroundings. Many YSOs, including Class I and Class II sources are observed at the edges of the ionized region. A noticeable massive Class 0 candidate is detected towards the highest density condensation (condensation 1), later confirmed with *Herschel* observations (Zavagno et al. 2010). A spectrophotometric study of the YSOs in the near-infrared confirm that these YSOs are associated with the RCW 120 region because they have the same velocity than that of the ionized gas (Martins et al. 2010).

DEH09 observed a series of eleven young sources aligned parallel to the ionization front towards the most massive condensation at $24\ \mu\text{m}$ equally spaced by 0.1 pc and is thought to be the result of Jeans gravitational instabilities.

Tremblin et al. (2014b) studied the probability density function (PDF) of a series of Galactic H II regions, including RCW 120 (see their fig. 8 and fig. 9). They found evidence for compression, and the value of the exponent derived to fit the PDF towards condensation one may indicate the role of ionization compression in the formation of this condensation and its collapse to form stars. According to numerical simulations lead by Minier et al. (2013), if the condensation had gravitationally collapsed prior to the passage of the ionization front, the condensation would be already sufficiently dense to resist the ionization front expansion. It would, for example, trigger the formation of a pillar rather than a condensation remaining in the shell.

Walch et al. (2015) performed three dimensional smoothed particle hydrodynamics (SPH) simulations of H II regions expanding into fractal molecular clouds and then used RADMC-3D to compute the synthetic dust continuum emission at $870\ \mu\text{m}$ from their simulations, applied to RCW 120. They found a hybrid form of triggering which combines elements of collect and collapse (C&C) mechanism (Elmegreen & Lada 1977) and radiation driven implosion (RDI) (Kessel-Deynet & Burkert 2003).

Figure 1 presents a three-color image of the RCW 120 region as seen by *Herschel*. The $70\ \mu\text{m}$ emission (blue part) underlines the emission of the warm dust while the $250\ \mu\text{m}$ emission (red part) underlines the emission from the colder dust located in the dense material that surrounds the ionized region and that interacts with the ionizing radiation.

3. Observations and data reduction

3.1. *Herschel* observations

RCW 120 was observed with the PACS and SPIRE photometers. Details of these observations (map size, observing time, obser-

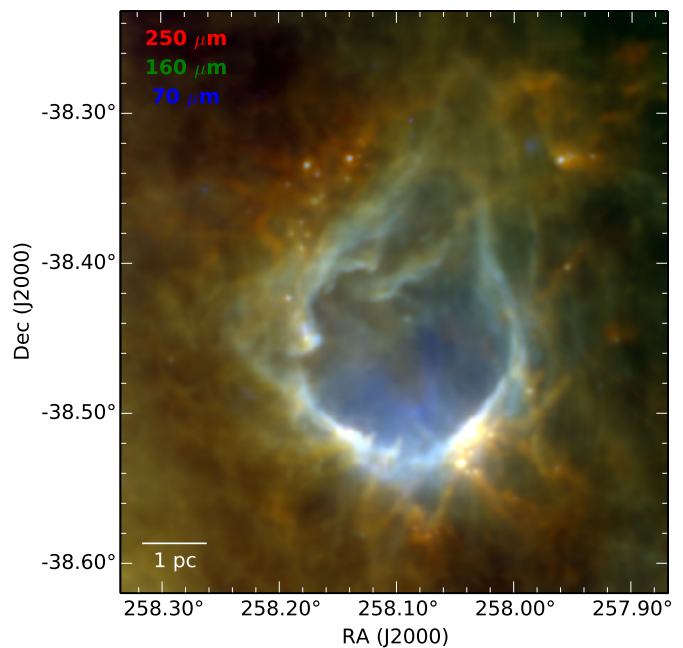


Fig. 1: RCW 120: *Herschel*-PACS $70\ \mu\text{m}$ (blue), $160\ \mu\text{m}$ (green) and *Herschel*-SPIRE $250\ \mu\text{m}$ (red). The field size is $21.8' \times 24.5'$. North is up, east is left

vational identification (ObsID), observational date (Obs.) operational day (OD), map center) are given in Table 1. The PACS photometer was used to make simultaneous photometric observations in two photometric bands as part of the HOBYS key program (Motte et al. 2010). Two cross-scan maps were done at angle 45° and 135° with a scanning speed of $20''/\text{second}$. This observing mode is described in Section 5.2 of the PACS Observers' Manual¹. The beam FWHM varies between $5''9$ at $70\ \mu\text{m}$, $6''0$ at $100\ \mu\text{m}$ and $11''4$ at $160\ \mu\text{m}$. The total observing time is 2.6 hours.

RCW 120 was observed with the SPIRE photometer as part of the Evolution of Interstellar Dust key program for the *Herschel* Science Demonstration Phase. The SPIRE photometer was used to make simultaneous photometric observations in the three photometer bands (250 , 350 and $500\ \mu\text{m}$). The map is made by scanning the telescope at a given scan speed of $30''/\text{second}$ along lines. Cross-linked scanning is achieved by scanning at 42° (Scan A angle) and then at -42° (Scan B angle). This ensures that the effect of $1/f$ noise on the map can be minimized and also leads to improved map coverage. This observing mode is described in details in the last version of the SPIRE Observers' Manual² in Section 3.1.2. One map at each scanning angle was obtained. The beam FWHM varies between $18''2$ at $250\ \mu\text{m}$, $25''2$ at $350\ \mu\text{m}$ and $36''6$ at $500\ \mu\text{m}$. The total observing time is 0.34 hour.

The PACS maps were produced using the HIPE Level 1 data and then version 21 of the Scanamorphos software package which performs baseline and drift removal before regridding (Roussel 2012). The SPIRE images were reduced using modified

¹ http://herschel.esac.esa.int/Docs/PACS/html/pacs_om.html

² http://herschel.esac.esa.int/Docs/SPIRE/html/spire_om.html#x1-310003.2, Version 2.2, November 29, 2010

Table 1: Summary of *Herschel* observational parameters

Map size ($'$)	Time (s)	ObsIDs	Date yyyy-mm-dd	OD	Map center J2000
PACS 100 and 160 μm observations					
30 \times 30	3302	1342183978, 1342183979	2009-09-17	127	17 ^h 12 ^m 23 ^s :10 –38° 27' 43''
30 \times 30	3302	1342185553, 1342185554	2009-10-10	148	17 ^h 12 ^m 30 ^s :59 –38° 27' 25''5
PACS 70 and 160 μm observations					
30 \times 30	2762	1342216585, 134216586	2011-03-22	677	17 ^h 12 ^m 23 ^s :21 –38° 27' 43''21
SPIRE observations					
22 \times 22	1219	1342183678	2011-03-22	121	17 ^h 12 ^m 18 ^s :80 –38° 27' 58''5

pipeline scripts of Version 10 of HIPE³, the *Herschel* Interactive Processing Environment. Each map direction (nominal and orthogonal) was first reduced individually to Level 1 data, correcting for effects such as temperature drifts and jumps, glitches and cooler burps. The individual maps were then combined to create one map (Level 2 data). Map reconstruction was done using the SPIRE default 'naive' mapmaking algorithm at the same time as a destriper module (including a median correction and in bright source mode). The default gridding of 6'', 10'', 14'' for the SPIRE wavelengths 250, 350, 500 μm was chosen. The fits output files for each SPIRE wavelength are in units of Jy/beam. For an absolute calibration of the SPIRE maps, the zeroPointCorrection task calculates the absolute offset for a SPIRE map, based on cross-calibration with Planck HFI-545 and HFI-857 maps, color-correcting HFI to SPIRE wavebands assuming a gray-body function with fixed spectral index. The offsets determined in this way correspond well to the ones provided by J.-P. Bernard (private communication).

3.2. Complementary data

We complement the *Herschel* data with data from the Two Micron All-Sky Survey (2MASS) at 1.25 μm (*J*), 1.65 μm (*H*) and 2.17 μm (*K_s*) with a resolution of 2'' (Skrutskie et al. 2006), from the *Spitzer*⁴ GLIMPSE and MIPS GAL surveys of the Galactic Plane at 3.6 μm , 4.5 μm , 5.8 μm and 8 μm and 24 μm with a resolution of 17'', 1''7, 1''9, 2'' and 6'' (Benjamin et al. 2003; Carey et al. 2009).

4. Data analysis

4.1. Compact sources' extraction method

Herschel compact sources were extracted using the multi-wavelength, multi-scales *getsources* algorithm⁵ (version 1.140127) (Men'shchikov et al. 2012; Men'shchikov 2013). The working method of *getsources* can be roughly decomposed into two steps : the detection and the measurement. While the latter is performed on all maps inserted into the algorithm, the detection can be made from a selected sample of maps depending on the aim of the study. In order to improve this step, an *Herschel* high-resolution density map (Hill et al. 2012; Palmeirim et al. 2013) was created (see Sect. 4.5) and added to

³ HIPE is a joint development software by the *Herschel* Science Ground Segment Consortium, consisting of ESA, the NASA *Herschel* Science Center, and the HIFI, PACS, and SPIRE consortia.

⁴ <http://irsa.ipac.caltech.edu/data/SPITZER>

⁵ The *getsources* algorithm is publicly available and can be downloaded at <http://www.herschel.fr/cea/gouldbelt/en/getsources/>

better constrain the detection of compact sources. Moreover, some original maps were modified in order to enhance the contrast of the cooler and hence the densest regions since heated structures could be detected and misleading the final sample of sources. For this purpose and to provide valuable guidance to the detection algorithm, we use the 160 μm PACS and 250 μm SPIRE maps as they represent a good compromise between resolution and non-contamination by very small grains (VSG). The photometric offsets derived using IRAS-PLANCK model (Bernard et al. 2010) were added and the 160 μm map was convolved to the resolution of the 250 μm SPIRE observations (25''2). We assumed a modified blackbody (hereafter, MBB) model with a spectral index of 2. This value is higher than the reference for the galaxy (~ 1.6 , Planck Collaboration et al. (2016)) but for dense regions, in the inner regions of the galactic plane for instance, β tends to increase and hence, a value of 2 should be more appropriate for compact regions (Paradis et al. 2012). Non-linear fitting of the SEDs was performed using the Levenberg-Marquardt's algorithm (Markwardt 2009). From the SED, a color temperature can be found for each pixel by using the ratio of the two maps

$$\frac{I_{250\mu\text{m}}}{I_{160\mu\text{m}}^{\theta=25''2}} = \left(\frac{\nu_{250\mu\text{m}}}{\nu_{160\mu\text{m}}} \right)^5 \frac{e^{\frac{h\nu_{160\mu\text{m}}}{kT}} - 1}{e^{\frac{h\nu_{250\mu\text{m}}}{kT}} - 1}, \quad (1)$$

where $I_{160\mu\text{m}}^{\theta=25''2}$ is the 160 μm map convolved at the 250 μm resolution.

A weight-map is then created as the ratio between the map giving the MBB flux corresponding to the color temperature and a fiducial temperature of 20 K (median temperature). Multiplying the native 160 μm PACS map by the weight-map give the 160 μm corrected map where colder regions are enhance compared to warmer regions. The 250 μm corrected map is created in the same way and both are used in replacement of the native 160 μm PACS and 250 μm SPIRE maps for the detection step.

To summarize, for extraction of the sources, we use the original 70 μm , 100 μm , 350 μm , 500 μm maps and improved the detection by including the high-resolution density map and the 160 μm and 250 μm corrected maps.

4.2. Pre-selection

The final *getsources* catalog contains many useful informations about the detected sources. In the following subsections, we will keep only a small part of them : J2000 coordinates, detection significance at each wavelength, flux at peak and integrated flux with their corresponding errors and source ellipse parameters (major axis, minor axis, position angle).

Before doing the analysis, the sources present in the catalog have to be filtered to select the well-defined ones. The selection criteria defined by the HOBYS consortium are listed below (see also Tigé et al. submitted) :

Each source must have a *deconvolved size* (see Eq. 2) smaller than 0.1 pc at the *reference wavelength* (see below) and three reliable fluxes (including the reference wavelength). A flux is considered as reliable if the detection is reliable (the detection significance is higher than 7, see Men'shchikov et al. 2012), the signal to noise of the peak and integrated flux is higher than 2 and the elongation (defined as the ratio of the major and minor axis of the ellipse footprint) lower than 2 in order to limit the sample to circular compact cores.

From these criteria, sources extracted by *getsources* are expected to be dense and cold. Therefore, we consider as a good assumption that thermal emission from the cores is optically thin and not contaminated by VSGs for $\lambda \geq 100 \mu\text{m}$. The *deconvolved size* at wavelength λ , θ_{deconv}^λ , is computed as

$$\theta_{deconv}^\lambda = \sqrt{\theta_{conv}^{a,\lambda} \times \theta_{conv}^{b,\lambda} - \text{HPBW}_\lambda^2}, \quad (2)$$

where $\theta_{conv}^{a,\lambda}/\theta_{conv}^{b,\lambda}$ stand for the major/minor convolved size estimate of the source at wavelength λ (given in the *getsources* catalog) and HPBW_λ is the half-power beam width at wavelength λ . The reference wavelength was chosen to be $160 \mu\text{m}$ as a compromise between the resolution ($11''.4$) and the tracer of optically thin dust emission. This trade-off allows for both the correct identification of the peak of the SED and a good scaling of the flux (Motte et al. 2010; Nguyen Luong et al. 2011). Nevertheless, in some marginal cases, the $160 \mu\text{m}$ emission may be contaminated by small grains heated in the photo-dissociation region (PDR) leading to a deconvolved size larger than the one measured at $250 \mu\text{m}$. In such cases, the $250 \mu\text{m}$ is taken as the reference (resolution $18''.2$).

Detections complying with the above-mentioned criteria were kept for the analysis. However, the $70 \mu\text{m}$ data were systematically excluded from the SED fitting to avoid contamination from VSG's emission even though the criteria were satisfied.

Among the 359 detections of the *getsources* algorithm, 80 were kept at the end of the selection (put in the pre-selected sample). Rejected sources appear to be false detections, mainly filament pieces or sources with not enough flux measurements to fit the SED. Rejected sources were visually inspected and those which look like compact sources with at least one reliable wavelength ($70 \mu\text{m}$ included) were kept in a tentative sample (80 sources). The physical properties of the tentative sources were derived throughout an indirect method (see Sect 5.2.4) since a SED fitting couldn't be done.

4.3. Spectral energy distribution

Before fitting the SED for each compact source, the fluxes must be scaled since we want them to be measured within the same aperture. A full treatment of this scaling can be found in Motte et al. (2010); Nguyen Luong et al. (2011) where the relation between flux and source's angular size is taken to be same as for protostellar cores. This aperture scaling is based on the assumptions that the source is optically thin for $\lambda > 100 \mu\text{m}$, $M(r) \propto r$ and the gradient of the temperature is weak within the region (Elia et al. 2014). The scaling was done when the size at the reference wavelength and the wavelength to be scaled could be deconvolved. Following their procedure, we applied scaling fac-

Table 2: Minimum, maximum and median values for the color correction factors at *Herschel* wavelengths for the final sample of sources

λ (μm)	Min	Max	Median
70	0.46	1.03	0.91
100	0.79	1.03	1.02
160	0.95	1.06	1.03
250	0.94	0.94	0.94
350	0.94	0.94	0.94
500	0.94	0.94	0.95

tors to fluxes according to the formula

$$S_\lambda^{\text{scaled}} = \zeta_\lambda \times S_\lambda = \frac{\theta_{deconv}^{\text{Ref}}}{\theta_{deconv}^\lambda} \times S_\lambda, \quad (3)$$

where $S_\lambda^{\text{scaled}}$ represents the rescaled flux associated with scaling factor ζ_λ and S_λ is the original flux.

The model to be fitted is a MBB (4) using the Hildebrand relation (Hildebrand 1983)

$$S_\nu(T) = \frac{M_{\text{env}} \kappa_{300\mu\text{m}}}{RD^2 \nu_0^2} \times \nu^\beta \times B_\nu(T) = C \times \nu^\beta \times B_\nu(T), \quad (4)$$

with a gas-to-dust ratio $R=100$, D the distance of RCW 120, 1.3 kpc, and C is introduced as a constant of the fit. The HOBYS consortium decided to use the dust opacity law $\kappa_\nu = \kappa_{300\mu\text{m}} (\nu/\nu_0)^2$ with $\kappa_{300\mu\text{m}}=10 \text{ cm}^2 \text{ g}^{-1}$, $\nu_0=1000 \text{ GHz}$ (Beckwith et al. 1990; Motte et al. 2010). As explained before, the spectral index has been fixed to two, reducing the model space of the fitting parameters to the C-T plane. The initial errors used to weight the data have been set to the quadratic sum of the *getsources* and the calibration errors (3% at $100 \mu\text{m}$, 5% at $160 \mu\text{m}$ and 7% for SPIRE bands).

During the acquisition of the sources with the PACS and SPIRE instruments of *Herschel*, the spectrum is assumed to be flat across the bands ($\nu S_\nu = \text{const}$) which is not true because we expect the sources to follow a MBB model. To correct for this assumption, we apply color correction factors given in the PACS and SPIRE observer's manual. The fitting algorithm reaches convergence when the absolute difference between two subsequent temperatures (obtained at two consecutive steps) is fainter than 0.1 K. Since the spectral index was fixed to two, these factors depend on the temperature for PACS and are constant for SPIRE. Table 2 gives the minimum, maximum and median value for the color correction factors at *Herschel* wavelengths. Color corrections are high for short wavelengths and low temperature. For $70 \mu\text{m}$ and $100 \mu\text{m}$, they go up to 54% and 21% and corresponds to a source with $T=11.2 \text{ K}$. However, considering the median value for all wavelengths, the color correction factors are low and do not change drastically the sources' fluxes of the final sample.

The final temperature is derived directly as one of the parameter of the MBB model and assuming optically thin emission for the dust, the envelope mass is derived as

$$M_{\text{env}} = R \frac{S_\nu(T) D^2}{\kappa_\nu B_\nu(T)} = C \times 8.496 \times 10^8 M_\odot. \quad (5)$$

The uncertainties are derived from the fitting errors and are 3% and 20% in average for the dust temperature and the envelope mass, respectively. Obviously, these error values on the physical parameters do not take into account the dependence of

β with the wavelength (from 1 to ≥ 2) and the uncertainty on the opacity factor which is at least a factor of two due to the unknown properties of dust grains (Deharveng et al. 2012, see their Sect 4.1).

Each detected YSO's bolometric luminosity was computed by integrating the corresponding SED curve. For sources having infrared (IR) counterparts (from the 2MASS, GLIMPSE and MIPS GAL surveys) within a radius of 4'', the SED was bipartitioned and partial integrations are made over it. Below 70 μ m, a so-called IR luminosity is obtained using a trapezoidal integration scheme (numerical integration done by connecting the data points with straight lines) from the first IR counterpart found in the catalogs to the 70 μ m flux. From 70 μ m onwards a so-called "Herschel luminosity" is obtained by integrating over the Herschel SED. The bolometric luminosity is obtained by adding these two values. The SED fitting algorithm returned the error on Herschel luminosity while that affecting the IR one is obtained by computing the IR luminosity with the fluxes plus the uncertainties (higher-limit) and with the fluxes minus the uncertainties (lower-limit). On average this resulted in an overall uncertainty of 30% on bolometric luminosity. The average volume density was computed by assuming a spherically symmetric core with a diameter equal to its deconvolved size at the reference wavelength

$$\langle n_{H_2} \rangle = \frac{M_{env}}{\frac{4}{3}\pi \times (\theta_{deconv}^{Ref})^3}. \quad (6)$$

After the SED fitting, a second stage selection was applied to obtain the final sample of sources discussed in this paper (described below).

4.4. Final selection

At the end of the SED fitting procedure, the sample of sources obeying our first-stage selection scheme (pre-selected sample) was visually inspected at each Herschel wavelength, to ensure the detection of truly compact sources. The requirements for a source to pass successfully this second-stage selection scheme are two-fold : (1) The source had to be clearly seen by eye on one of the Herschel images, and (2) The source's SED had to be well-constrained.

The first condition was checked by two different people to avoid subjective detections. The second condition allows us to eliminate dubious SED, for example SED with unconstrained peak or SED with increasing flux mostly at SPIRE wavelengths. From this second stage selection, 35 sources were kept for the study (final sample), seven sources having unconstrained SED were added to the tentative sample and 38 sources looking like small clumps or filamentary pieces were rejected.

To summarize the two-stage selection : from the 359 detections, 35 sources are included in the final sample and 87 sources are included in a tentative sample. The latter is composed of sources possessing at least one reliable wavelength (including 70 μ m) clearly seen (by eye) in the Herschel images but not pre-selected due to the lack of flux measurements or pre-selected sources whose SED is unconstrained. These detections are thought to be real sources and kept in order to derive their physical properties with an indirect method since their SED cannot be used.

The second-stage selection is definitely highly non-conservative but ensures the reliability of the sources to be investigated. As discussed before, part of the remaining detections could be real sources under filaments with well-constrained

SED which are eliminated in order to have a reliable sample of sources. Finally, we are left with two samples : the final one which will be discussed in the paper and the tentative one whose physical parameters will be derived with an indirect method. We assume that the selected sources are associated with RCW 120, that is, they are located at the same distance. This assumption is supported by the study by Martins et al. (2010) who showed using high resolution near-IR spectro-photometric observations that the YSOs with a IR counterpart observed towards RCW 120 are at the same velocity as that of the ionized gas. We further discuss this point in Sect. 5.2.2.

4.5. Dust temperature and column density maps

4.5.1. Method

Following the procedure of Hill et al. (2011, 2012), a map of dust temperature at 36''6 can be obtained by fitting the flux at each pixel, using the MBB model

$$F_\nu = \frac{B_\nu(T_{dust})\kappa_\nu\Sigma_{500\mu m}}{R} = \frac{B_\nu(T_{dust})\kappa_\nu\mu m_H N(H_2)}{R}, \quad (7)$$

where F_ν is the brightness, μ the mean molecular weight (≈ 2.8), m_H the proton mass and $N(H_2)$, the column density. The temperature and the gas surface density $\Sigma_{500\mu m}$ (the 500 μ m subscript stands for the corresponding resolution) are the fitting parameters. Another direct byproduct of the fitting algorithm is a map of the H_2 column density at the same low-resolution assuming the dust opacity law of Beckwith et al. (1990) (See Sect. 4.3). Since most of the observed regions through the HOBYS project are not observed at 100 μ m, the method considers only wavelengths higher than 160 μ m for the SED fitting even if the data were available. This choice made the comparison of temperature and column density maps obtained for different regions easier.

Following the procedure described by Palmeirim et al. (2013) based on a multi-scale decomposition method, a high-resolution column-density map at 18''2 can be computed. The gas surface density smoothed at 250 μ m resolution ($\Sigma_{250\mu m}$) can be written as a sum of gas surface density smoothed at 350 μ m ($\Sigma_{350\mu m}$) and 500 μ m resolution

$$\Sigma_{250\mu m} = \Sigma_{500\mu m} + (\Sigma_{350\mu m} - \Sigma_{500\mu m}) + (\Sigma_{250\mu m} - \Sigma_{350\mu m}). \quad (8)$$

The second term in parentheses of Eq. 8 represents the spatial scale structure of the region seen at 350 μ m without the largest structure corresponding to the 500 μ m observations. An estimate of $\Sigma_{500\mu m}$ can be obtained by considering that these data are approximately equal to $\Sigma_{350\mu m} * G_{350-500}$ where $G_{350-500}$ is the full width at half maximum (FWHM) of the point spread function (PSF) needed to convolve the 350 μ m map to the 500 μ m resolution ($\sqrt{36''6^2 - 25''2^2} = 27''2$). The gas surface density $\Sigma_{350\mu m}$ is obtained in the same way than $\Sigma_{500\mu m}$ but excluding the 500 μ m data from the SED fitting.

The third term of Eq. 8 represents the structure seen at 250 μ m without the largest scale structure seen at 350 μ m. As before, $\Sigma_{350\mu m}$ can be written as $\Sigma_{250\mu m} * G_{250-350}$ and $\sqrt{25''2^2 - 18''2^2} = 17''4$ is the FWHM of the PSF needed. The gas surface density $\Sigma_{250\mu m}$ is obtained using the ratio of the 160 μ m and 250 μ m maps as explained in Sect 4.1. Finally, Eq. 8 can be rewritten as

$$\Sigma_{250\mu m} = \Sigma_{500\mu m} + (\Sigma_{350\mu m} - G_{350-500} * \Sigma_{350\mu m}) + (\Sigma_{250\mu m} - G_{250-350} * \Sigma_{250\mu m}). \quad (9)$$

Hence, the resulting high-resolution density map can be seen as a composite map representing the multi-scale structure of RCW 120 from $250\ \mu\text{m}$ to $500\ \mu\text{m}$ resolution.

4.5.2. Comparison with Anderson et al. (2012) maps

Anderson et al. (2012) constructed temperature and column density maps for a sample of H II regions (Sh 104, W5-E, Sh 241, RCW 71, RCW 79, RCW 82, G332.5-0.1 and RCW 120). Two differences exist between the method he used and the one we used (also described in Hill et al. (2012)). In the method used by Anderson et al. (2012), the SED is fitted with all the data available (from $70\ \mu\text{m}$ to $500\ \mu\text{m}$) and a flat background is subtracted in each *Herschel* map (see also Battersby et al. (2011)). In warm regions (the ionized zone typically) where $70\ \mu\text{m}$ and $100\ \mu\text{m}$ fluxes are high (around $3 \times 10^3\ \text{MJy sr}^{-1}$), the inclusion of these data in the fit induces a shift of the SED towards the high-frequency region and increases the temperature. The cold regions are less affected because the $70\ \mu\text{m}$ and $100\ \mu\text{m}$ fluxes are lower (around $3 \times 10^2\ \text{MJy sr}^{-1}$). Spectral energy distributions representing both case for pixels giving a high and low temperature are shown in Figure 2. In hot regions, the difference in temperature reaches 4 K (18%) while it is only 2 K (14%) for cold regions.

To make a comparison between the temperature maps obtained using each method, we resample them at $14''\text{pix}^{-1}$ to the same center and compute their ratio to see how the different methods lead to different temperature in specific regions (see Fig. 3a). The structure seen on these images clearly reproduces the egg-shaped of RCW 120 and shows that the differences occur in specific regions. We define an area in the warmest (around the ionizing star) and coldest region (defined as condensation 5 hereafter) and compute the median and the standard deviation for them and the whole map. Results are shown in Table 3 where HR and CR stand for hot and cold regions. From the first and third line, we see, as expected, that the temperature found is higher when the $70\ \mu\text{m}$, $100\ \mu\text{m}$ and background subtraction are included particularly for the warmest region where the change is around 6 K. The colder region do not present significant difference ($\approx 0.2\ \text{K}$).

To estimate the change in temperature induced by the background subtraction, we created another temperature map using the method of Anderson et al. (2012) (including the $70\ \mu\text{m}$ and $100\ \mu\text{m}$ data points) but without removing any background. The range of temperature for this method is listed in the second line of Table 3. We note, as expected, that hot regions are more affected by the inclusion of high-frequency maps ($\approx 2\ \text{K}$) and by the background subtraction ($\approx 5\ \text{K}$). The error on the fit for the temperature map has a mean value of 0.45 K hence the temperature for cold regions remains roughly the same.

The comparison between the two column density maps is less straightforward since Anderson et al. (2012) used only the $350\ \mu\text{m}$ to obtain this map while our is the byproduct of the SED fitting. On Fig. 3b, the ratio of the column density map shows that warm regions are more affected than colder ones. Due to the anticorrelation between column density and temperature, we expect warm regions to be more affected with the inclusion of the $70\ \mu\text{m}$ and the $100\ \mu\text{m}$ fluxes. Moreover, since the flux is linear with the column density to first order, we expect the background to be roughly equal for all the regions. Table 4 presents the values of column density for the whole map, the densest region (condensation 1 defined hereafter) and an area in the north-west of RCW 120 where the density is low (empty region) using the three different methods. Trends can be seen: as we include high frequency maps and background subtraction, the median

Table 3: Range for the temperature map constructed following the method described in Hill et al. (2012) (first line), with all wavelengths and no background subtraction (second line) and following Anderson et al. (2012) (third line) for the whole map (first and fourth columns), the hottest region (second and fifth columns) and coldest region (third and sixth columns)

Method	Median (K)			σ (K)		
	Map	HR	CR	Map	HR	CR
$160\ \mu\text{m}$ - $500\ \mu\text{m}$, no BS	18.5	23.1	16.4	1.2	0.9	0.4
$70\ \mu\text{m}$ - $500\ \mu\text{m}$, no BS	17.9	24.7	16.2	1.6	0.82	0.4
$70\ \mu\text{m}$ - $500\ \mu\text{m}$, BS	20.0	29.2	16.2	2.7	1.6	1.0

Table 4: Range for the column density map constructed following the method described in Hill et al. (2012) (first line), with all wavelengths and no background subtraction (second line) and following Anderson et al. (2012) (third line) for the whole map (first and fourth columns), the densest region (second and fifth columns) and empty region (third and sixth columns)

Method	Median ($10^{22}\ \text{cm}^{-2}$)			σ ($10^{22}\ \text{cm}^{-2}$)		
	Map	DR	ER	Map	DR	ER
$160\ \mu\text{m}$ - $500\ \mu\text{m}$, no BS	1.9	8.6	0.9	1.5	8.1	2.1
$70\ \mu\text{m}$ - $500\ \mu\text{m}$, no BS	1.5	4.4	1.1	0.8	3.5	0.2
$70\ \mu\text{m}$ - $500\ \mu\text{m}$, BS	0.4	3.0	0.3	0.6	0.3	0.2

column density decreases. The $70\ \mu\text{m}$ and the $100\ \mu\text{m}$ fluxes lead to a difference of $4 \times 10^{21}\ \text{cm}^{-2}$ for the warm region and does not change significantly the column density for cold ones. Removing the background causes a loss in column density of $1 \times 10^{21}\ \text{cm}^{-2}$. The method described in Hill et al. (2012) was the choice of the HOBYS consortium for the construction of temperature and column density maps and consequently, no background subtraction is made. This rule will allow an unbiased comparison between the different regions observed in the HOBYS project.

5. Results

5.1. Dust temperature and column density maps

Fig. 4 presents the temperature map obtained for RCW 120 with labelled condensations of DEH09 defined by yellow contours. The temperature ranges from 15 K to 24 K. Temperatures between 19 K and 24 K are observed towards the ionized region, the highest temperature being observed to the south. A colder medium with a temperature around 15-18 K surrounds the H II region. This colder medium is highly structured, organized in clumps, filaments and condensations that correspond to the condensations defined in DEH09 where the sources are located. A remarkable feature is the sharp edge seen on the temperature map at the south-western border of the ionized region. This drop in temperature (from 21 K to 16 K) corresponds to the presence of the (sub)millimeter condensation 1.

Fig. 5a presents the low resolution ($36''6$) column density map with the condensations of DEH09 and Fig. 5b the high-resolution column density map ($18''2$) together with H α emission from the SuperCosmos H α survey (Parker et al. 2005). The values range from $7 \times 10^{21}\ \text{cm}^{-2}$ to $4 \times 10^{23}\ \text{cm}^{-2}$ for the low-resolution map and goes up to $9 \times 10^{23}\ \text{cm}^{-2}$ for the high-resolution one. We checked that the convolution of the high resolution column density map to $36''6$ with the same grid agrees with the values found for the low resolution one. As expected, the ionized region with its egg-shaped corresponds

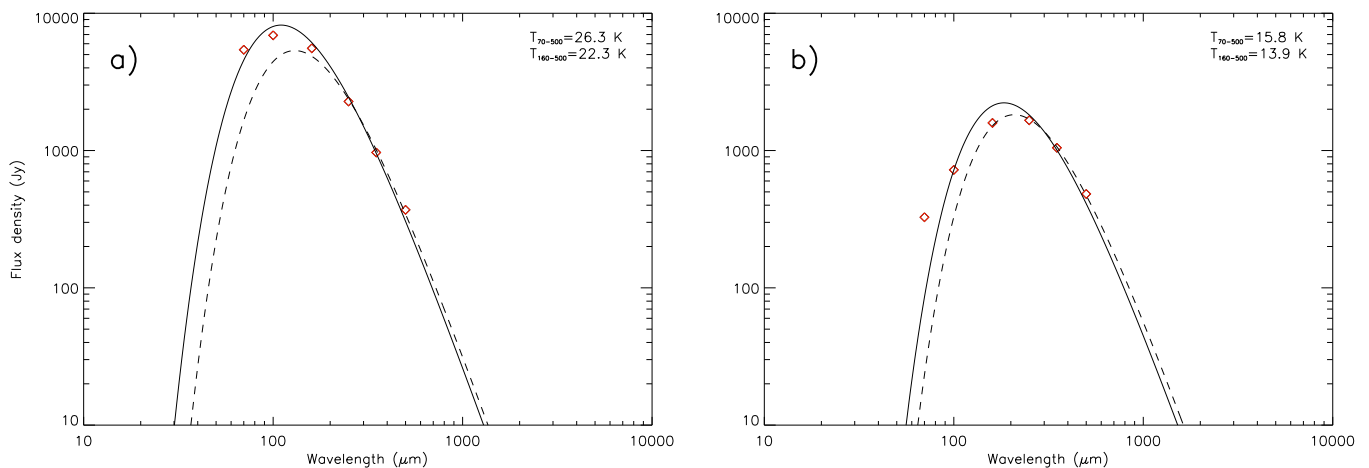


Fig. 2: (a) SED fitting for the pixels giving the highest temperature. The continuous curve represents the fit made with all *Herschel* fluxes and dashed curved is the fit obtained by the method of Hill et al. (2012). (b) Same for the pixel giving the lowest temperature. No background is subtracted in both cases

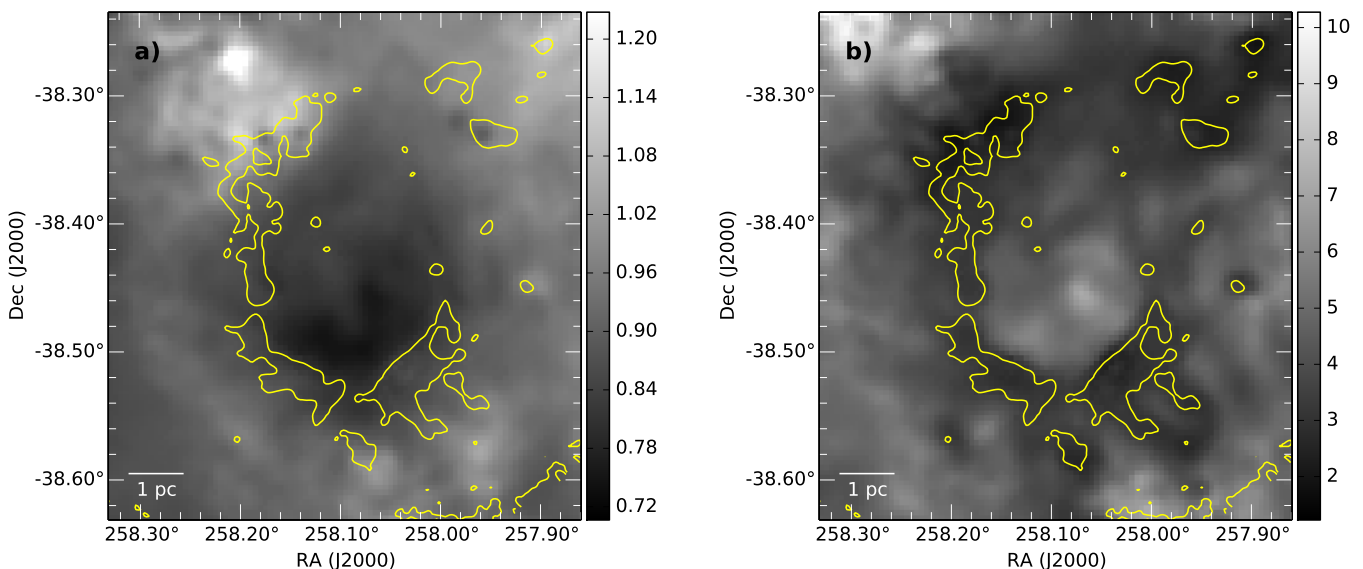


Fig. 3: (a) Ratio of temperature between the maps obtained in this paper (no $70\ \mu\text{m}$ and $100\ \mu\text{m}$ data included and no background subtraction) over the ones obtained by Anderson et al. (2012) (see text). The yellow contours correspond to $870\ \mu\text{m}$ emission at $0.1\ \text{Jy/beam}$. (b) Same but with the column density maps

to a drop in column density compared to the PDR and low column density filaments ($N(\text{H}_2) = 1.7 \times 10^{22}\ \text{cm}^{-2}$) are observed within it. These are seen in absorption in the optical (see fig. 1 in ZAV07) and show some compact structures that host sources (see Fig. 7 and Sect. 5.2). Around the ionized region, a highly structured material is distributed in filaments and clumps where the nine condensations already observed at $1.3\ \text{mm}$ (ZAV07) and $870\ \mu\text{m}$ (DEH09) are well seen. The leaking of the UV flux presented in DEH09 (see their fig. 16) is also seen on Fig. 5b. It creates the extended elliptical structures observed on the southern part of the ionized region together with the structures observed on the north-eastern and north-western parts. Three pre-stellar clumps are seen on the temperature and density maps at $(\alpha, \delta) = (257^\circ 91', -38^\circ 28')$, in absorption on the 70 and $100\ \mu\text{m}$ images and in emission at $160\ \mu\text{m}$ onward (see Fig. 5a). In general, the size and elongation of these clumps are too large to be part of the studied sample but their detection at

SPIRE wavelengths (and at $870\ \mu\text{m}$, see Fig. 2 in DEH09) suggests that they are pre-stellar clumps. The contrast between the high and low density regions is equal to 60. The highest density is observed in condensation 1 located at the south-western edge of the ionized region. This condensation could have been formed due to compression from the ionization region (Tremblin et al. 2014b). Towards RCW 120, star formation is observed in column density region higher than $2.2 \times 10^{22}\ \text{cm}^{-2}$.

5.2. Compact sources

5.2.1. Compact sources' spatial distribution

Figure 6 shows the 35 selected sources superimposed on a PACS $70\ \mu\text{m}$ gradient-filtered image of RCW 120. This image was produced with a standard 3×3 bi-directional Sobel-Feldman convolution kernel applied to the original image. For each pixel,

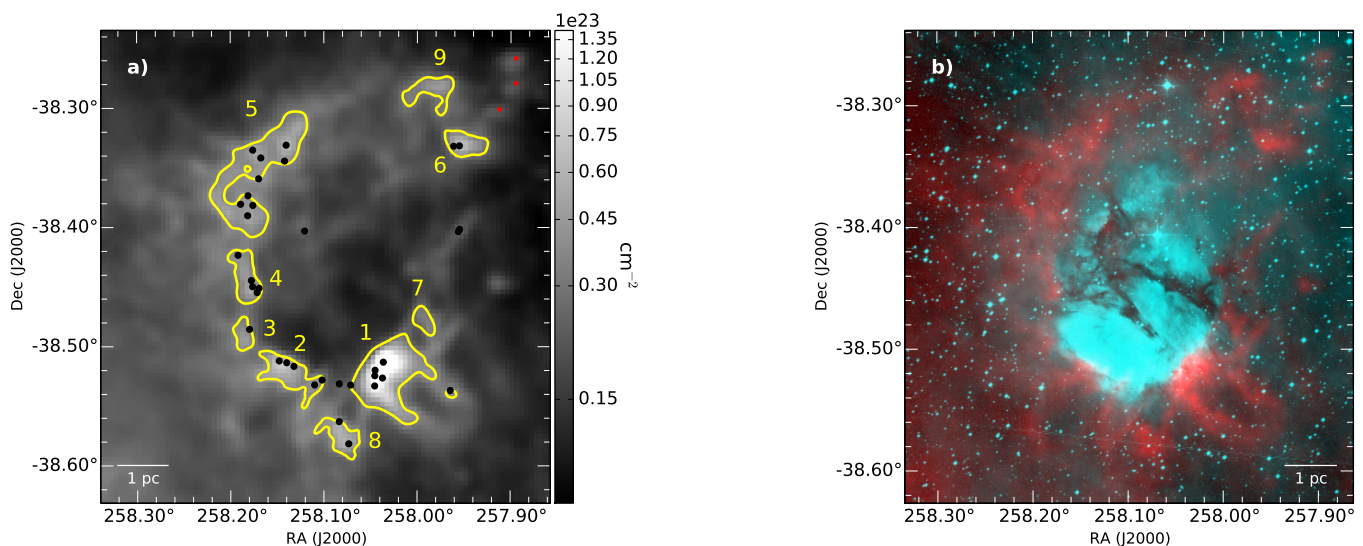


Fig. 5: (a) On logarithmic scale, H₂ column density map of RCW 120 at 36''6 resolution with 870 μm emission from LABOCA (in yellow contours), the final sample of sources (black dots) and the three prestellar clumps (red dots). Condensations observed at 870 μm are identified following the labelling in DEH09. The density values range from $7 \times 10^{21} \text{ cm}^{-2}$ to $4 \times 10^{23} \text{ cm}^{-2}$. (b) High resolution H₂ column density map of RCW 120 at 18''2 resolution (in red) and H α emission (in blue) from the SuperCOSMOS H α Survey. The column density values range from $7 \times 10^{21} \text{ cm}^{-2}$ to $9.4 \times 10^{23} \text{ cm}^{-2}$.

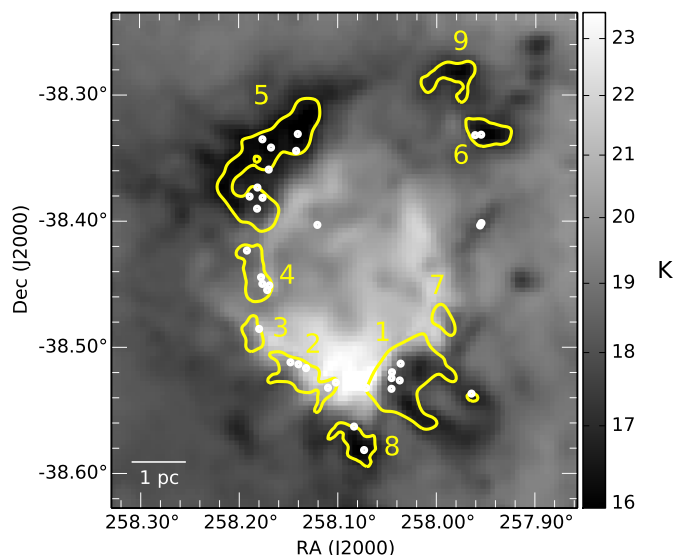


Fig. 4: Temperature map of RCW 120 at 36''6 resolution with 870 μm emission from LABOCA (in yellow contours) and the final sample of 35 compact sources (white dots) discussed in this paper. Condensations observed at 870 μm are identified following the labelling in DEH09. The temperature ranges from 15 K (dark) to 24 K (white). Warm regions are observed towards the ionized zone. Colder regions are located outside the ionized region and are distributed in cores, filaments and condensations

the derivatives along the horizontal ($\frac{\partial f}{\partial x}$) and vertical ($\frac{\partial f}{\partial y}$) directions are obtained and the final value for each pixel is computed as $\sqrt{(\frac{\partial f}{\partial x})^2 + (\frac{\partial f}{\partial y})^2}$ giving an approximate value of the gradient norm. This gradient-filtering cuts-off the diffuse emission and enhances the contrast of steep emission regions. In the following we define the PDR as the filamentary emission region revealed

by this gradient-filtering and shown by the green dashed contour seen in Fig. 7.

Using the selection criteria described in Sect. 4 and a visual inspection as a final check, we end up with 35 sources that are discussed (i.e., sources for which the temperature, envelope mass and bolometric luminosity can be derived). 87 additional detected sources are also shown in Fig. 7 but have less than two reliable fluxes (up to three if the 70 μm is included) or have unconstrained SEDs, meaning that their properties cannot be derived using SED fitting. Their original fluxes (given by *getsources* without any aperture scaling or color-corrections) are given in Table A.1.

As seen on Fig. 6, 14 sources are located outside the PDR and 21 are inside.

5.2.2. Compact sources' association with the region

Spectroscopic observations with SINFONI at the ESO-VLT showed the YSOs detected in the near IR towards RCW 120 have the same velocity as that of the ionized gas ($\approx -8 \text{ km s}^{-1}$) and are thus associated with RCW 120 (Martins et al. 2010). Even though most of the sources are thought to be part of RCW 120 because they are embedded in its filamentary region, sources located outside the PDR might not be associated with the region.

Studying the $J = 0 \rightarrow 1$ transition of ^{12}CO , ^{13}CO , C^{18}O and C^{17}O with the ATNF Mopra 22 m radio telescope, Anderson et al. (2015a) identified three emission peaks at -7 km s^{-1} (main temperature peak around the velocity of the ionized gas), -30 km s^{-1} and -60 km s^{-1} . The $J = 0 \rightarrow 1$ emission from the CO isotopologues (Anderson et al. 2015a) integrated between -75 km s^{-1} and -50 km s^{-1} , -35 km s^{-1} and -15 km s^{-1} and -15 km s^{-1} and $+3 \text{ km s}^{-1}$ are presented in Fig. 8 for ^{12}CO , Fig. 9 for ^{13}CO and Fig. 10 for C^{18}O . We point out that, contrary to the other maps in this paper, these figures are given in galactic coordinates.

Condensation 6, the northern-part of condensation 5 and sources 55 and 150 (the western part, between condensation 6 and 7) are

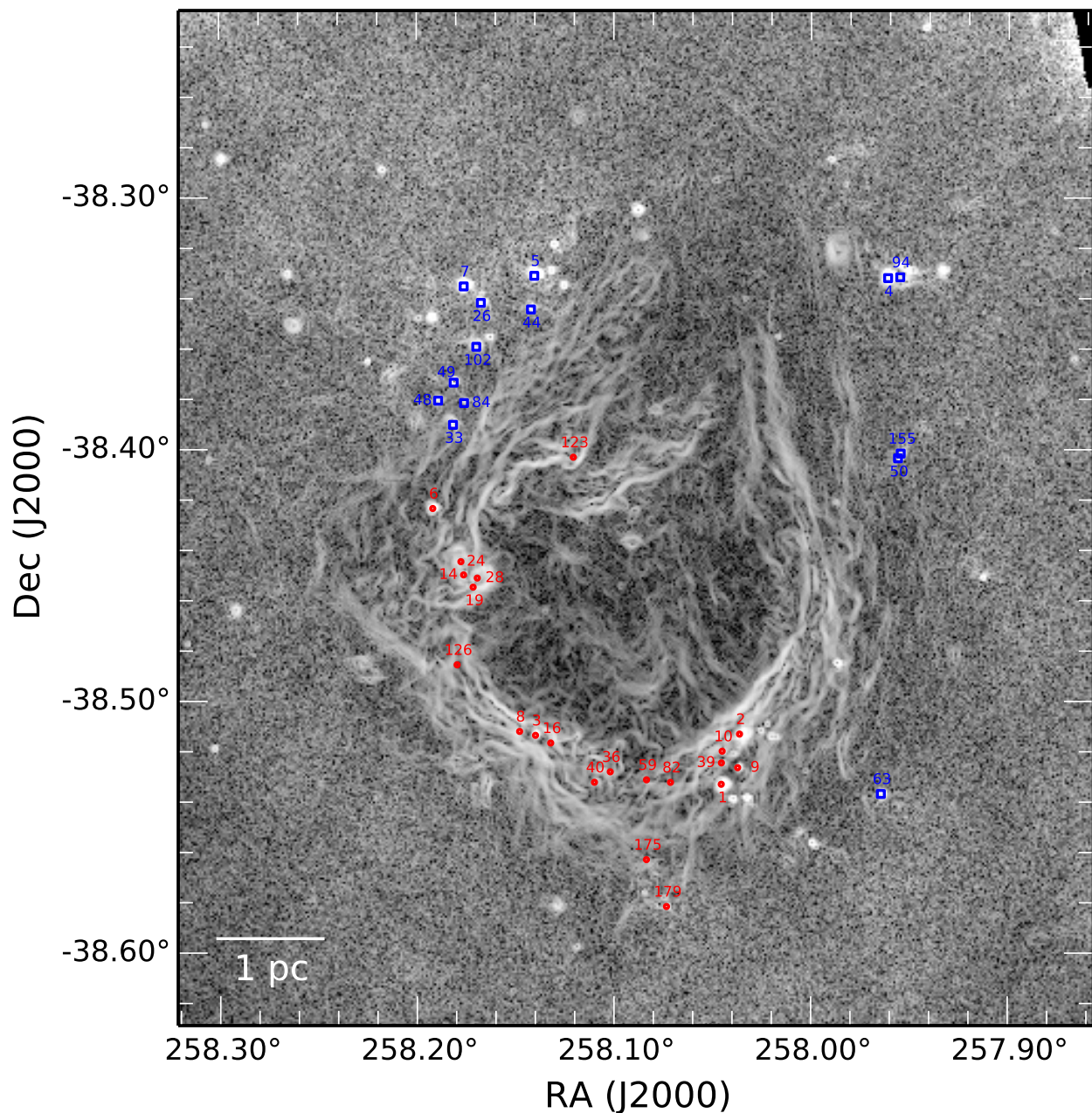


Fig. 6: All 35 compact sources detected using *getsources* (and discussed in the text) superimposed on a $70\mu\text{m}$ gradient image of RCW 120. The sources are color-coded depending on their location: red circles for sources observed towards the PDR, blue squares for sources outside (see text)

located outside the PDR but present an emission peak around -15 km s^{-1} and $+3\text{ km s}^{-1}$ which indicates that they are part of RCW 120. Condensation 9 presents an emission peak in the same range but also between -35 km s^{-1} and -15 km s^{-1} . Although we cannot rule out the fact that condensation 9 might be in the foreground or background of the region, the emission peak is stronger in the main-peak velocity range and therefore, we consider this condensation to be part of RCW 120. Between -15 km s^{-1} and $+3\text{ km s}^{-1}$, the other condensations are distributed along the strong CO emission, following the PDR that surrounds the ionized region. This strongly suggests that the 35 sources of the final sample are indeed associated with RCW 120.

5.2.3. Compact source properties

We have shown that the detected sources are likely to be associated with RCW 120, that is, located at the same distance (see Sect. 5.2.2). Table 5 gives the physical properties derived for the 35 sources: the *getsources* identification number (identification number in DEH09 given in parenthesis if any), the envelope temperature T , envelope mass M_{env} , bolometric luminosity L_{bol} , ratio of the submillimetric luminosity (defined as the luminosity computed from $350\mu\text{m}$ onwards) over the bolometric luminosity, ratio of the envelope mass over the bolometric luminosity, associated condensation towards which the source is observed, evolutionary class derived from the study of DEH09 and from

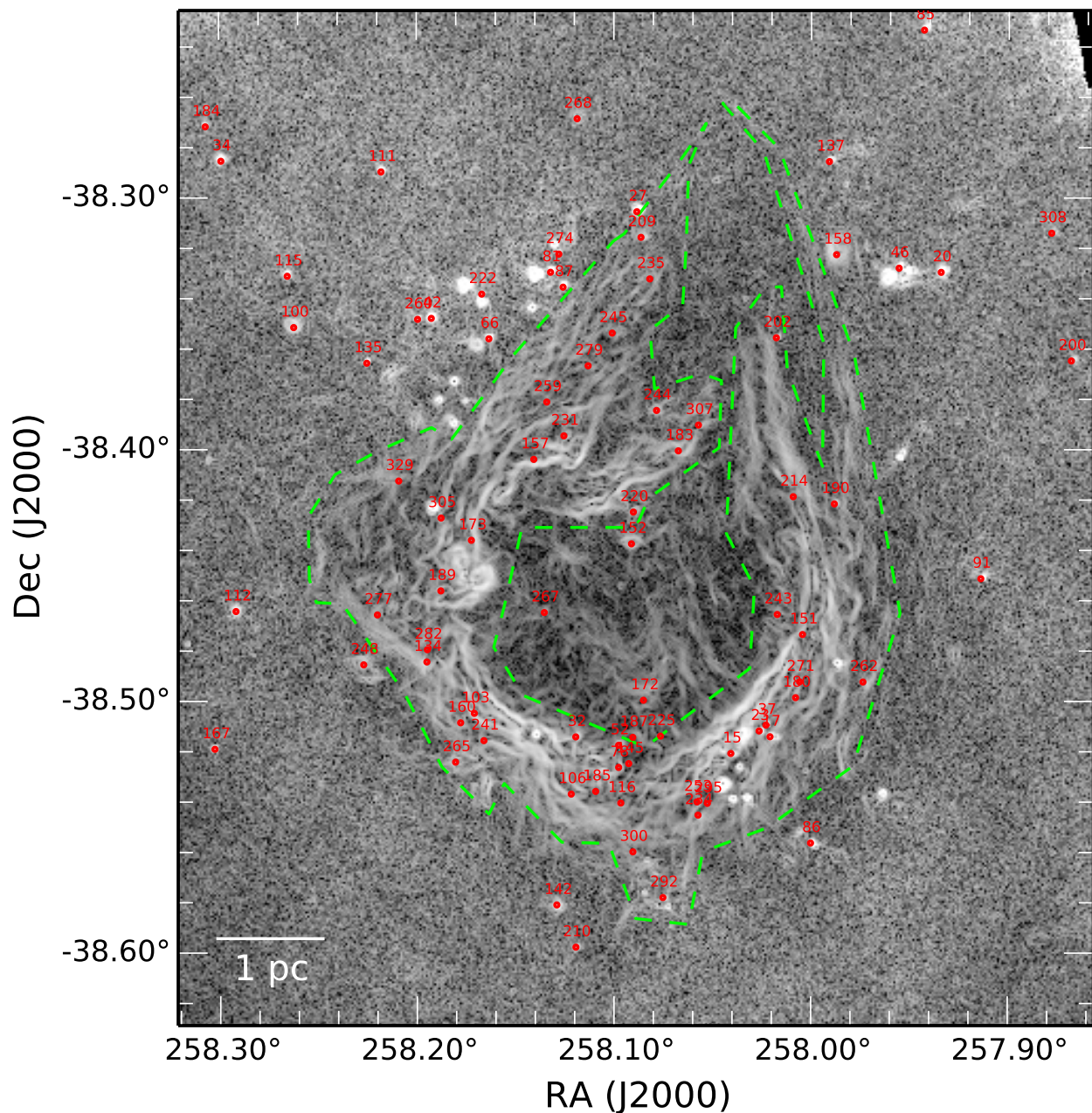


Fig. 7: All 87 sources detected by *getsources* but not part of the final sample due to the lack of reliable flux measurements, mainly at SPIRE wavelengths. Physical parameters of these sources are derived in a secondhand way explained and presented in Sect. 5.2.4. The PDR region is enclosed in the green contours (see text)

$L_{\lambda \geq 350 \mu\text{m}}/L_{\text{bol}}$, near- and mid-infrared counterparts, and volume density.

tors. A higher value of β better represents denser regions (Paradis et al. 2012).

In the following, source ID refers to IDs given in column 1 of Table 5 and Table A.1. Among the 35 sources of the final sample, 14 match the previous list discussed in DEH09. The sources previously identified on the basis on GLIMPSE and MIPS GAL data are now identified at *Herschel* wavelengths, based on their spatial correspondance in a radius of 4". We discuss their evolutionary class in Sect. 6. Adopting $\beta = 1.6$ from the latest *Planck* results, modifies the physical parameters (envelope temperature, envelope mass and bolometric luminosity) by 10% in average throughout the MBB model and color corrections fac-

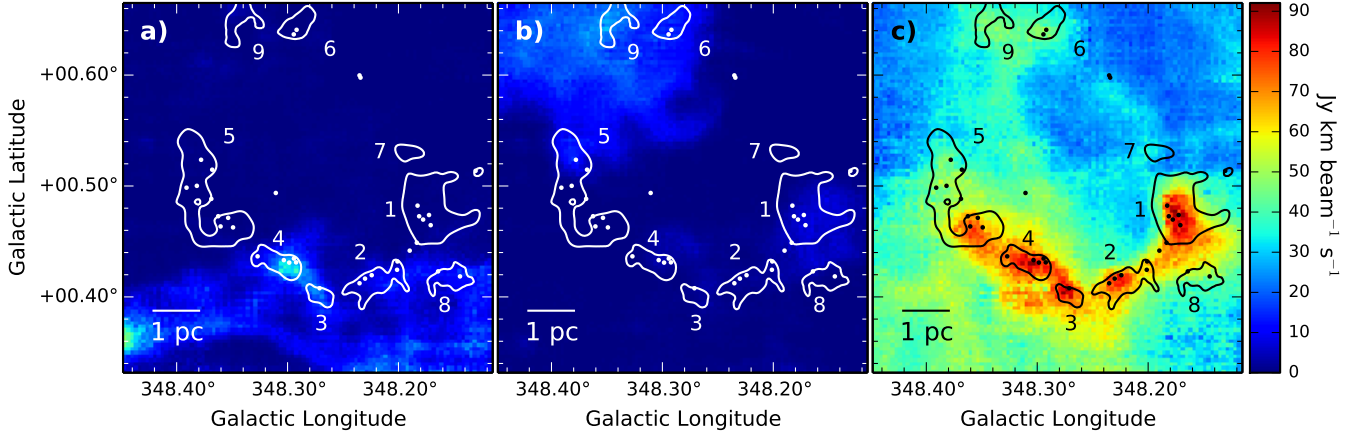


Fig. 8: Integrated intensity of ^{12}CO ($J = 0 \rightarrow 1$) between (a) -75 km s^{-1} and -50 km s^{-1} (b) -35 km s^{-1} and -15 km s^{-1} (c) -15 km s^{-1} and 3 km s^{-1} . The dots represent the 35 sources of the final sample and the contours stand for the $870 \mu\text{m}$ condensations of DEH09. The unit of the color image is in $\text{Jy km s}^{-1} \text{ beam}^{-1}$

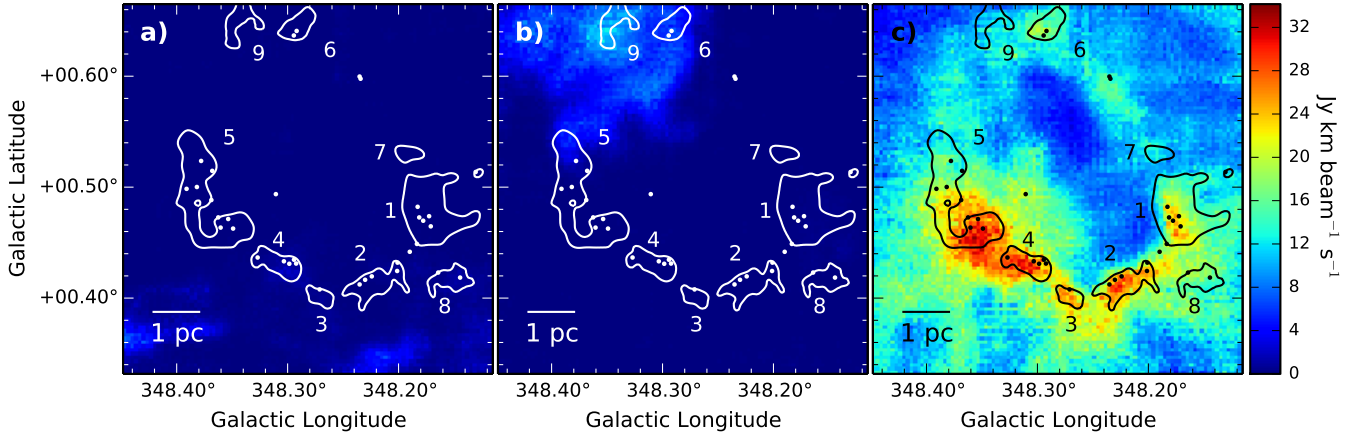


Fig. 9: Integrated intensity of ^{13}CO ($J = 0 \rightarrow 1$) within the same velocity ranges. Dots and contours are the same as in Fig. 8

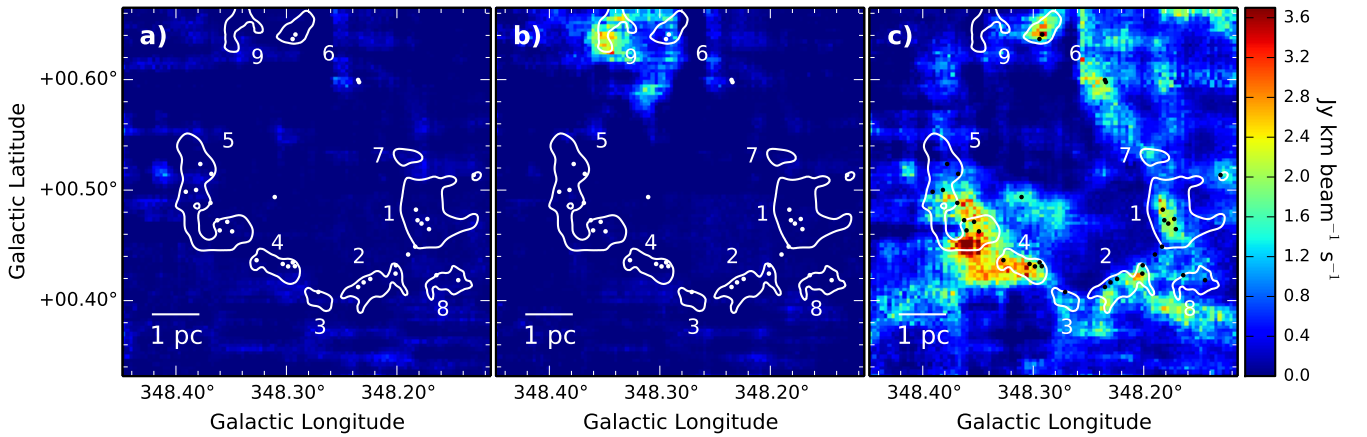


Fig. 10: Integrated intensity of C^{18}O ($J = 0 \rightarrow 1$) within the same velocity ranges. Dots and contours are the same as in Fig. 8

ID ^a	T ^b (K)	M _{env} ^c (M _⊙)	L _{bol} ^d (L _⊙)	M _{env} /L _{bol}	L _{λ≥350μm} /L _{bol} (%)	Cond ^e	Class (DEH09) ^f	L _{λ≥350μm} /L _{bol} ^g	IR ^h	<ρ _{H₂} > ⁱ (cm ⁻³)
1(38)	19.8	36	281	0.13	1.78	1	I	0-I	3.6 μm to 24 μm	>2×10 ⁷
2	20.3	174	1163	0.15	2.17	1		0-I		>1×10 ⁸
3(50)	20.9	14	167	0.08	1.26	2	I	0-I	2.17 μm to 24 μm	>8×10 ⁶
4(106)	19.1	9	92	0.1	1.22	6	I-flat?	0-I	2.17 μm to 24 μm	>5×10 ⁶
5(107)	17.3	11	77	0.14	1.42	5	I-II?	0-I	1.65 μm to 24 μm	>6×10 ⁶
6(76)	23.2	1	76	0.02	0.36	4	I-II?	I	1.65 μm to 24 μm	>9×10 ⁵
7(105)	20.9	3	36	0.09	1.42	5	I	0-I	3.6 μm 4.5 μm 5.8 μm 24 μm	>2×10 ⁶
8	16.4	30	58	0.53	4.86	2		0		>2×10 ⁷
9(40)	13.3	126	68	1.8	9.82	1	I	0	3.6 μm to 24 μm	2×10 ⁶
10	13.8	86	69	1.24	7.44	1		0	4.5 μm	2×10 ⁷
14(69)	19.2	16	97	0.16	2.13	4	I	0-I	1.25 μm to 24 μm	>1×10 ⁷
16	24.5	5	115	0.05	1	2		0-I	**	1×10 ⁶
19(67)	21.6	4	85	0.05	0.85	4	II	I	1.25 μm to 24 μm	1×10 ⁶
24(ObjectA)	26.9	2	86	0.03	0.68	4		I	5.8 μm to 24 μm *	>4×10 ⁵
26(103)	21.1	1	17	0.03	0.53	5	I-II?	I	1.25 μm to 24 μm	>3×10 ⁵
28(ObjectB)	34.1	1	212	0.01	0.24	4		I	1.25 μm to 24 μm *	>2×10 ⁵
33(88)	17.3	4	12	0.31	3.19	5	I	0	2.17 μm to 24 μm	>2×10 ⁶
36	27.1	1	28	0.03	0.66	2 bis		I	**	>4×10 ⁵
39	12.6	77	32	2.4	11.34	1		0	**	>1×10 ⁷
40	15.7	11	16	0.69	5.72	2 bis		0		>7×10 ⁶
44	18.3	1	6	0.23	2.66	5		0-I	All except 8 μm	>9×10 ⁵
48	19.7	1	7	0.14	1.95	5		0-I	24 μm	>6×10 ⁵
49(91)	19.6	1	7	0.11	1.46	5	I	0-I	1.65 μm to 24 μm	>5×10 ⁵
50	18.1	2	7	0.3	3.39	Fil.		0		>1×10 ⁶
59	20.8	2	16	0.13	1.97			0-I	**	>1×10 ⁶
63(37)	12.7	16	13	1.17	5.61	Fil	I-II?	0	3.6 μm to 24 μm	>1×10 ⁷
82	18.6	3	12	0.25	3.04	1		0-I		>1×10 ⁶
84	18.2	2	5	0.28	3.31	5		0-I		>9×10 ⁵
94	11.9	70	41	1.69	6.71	6		0	2.17 μm to 24 μm	>4×10 ⁷
102	18.7	3	15	0.18	2.22	5		0-I	1.65 μm to 24 μm	>2×10 ⁶
123	20	2	10	0.16	2.28			0-I		3×10 ⁵
126	23.4	2	31	0.06	1.22	3		0-I		>2×10 ⁵
155(86)	15.1	2	5	0.42	3.13	Fil.	I	0	1.25 μm to 24 μm	>1×10 ⁶
175	13.3	9	5	1.78	9.6	8		0	1.25 μm to 24 μm	>5×10 ⁶
179	11.2	45	9	5.23	17.53	8		0		>3×10 ⁷

Table 5: Properties of the 35 compact sources discussed in the text

^a Identification number given by *getsources* (corresponding identification number in DEH09 if present)

^b Temperature derived using the SED fitting with a MBB model

^c Mass of the core using the Hildebrand model (See Sect 4.3)

^d Luminosity computed from the lowest IR counterpart (if present) to the end of the SED

^e Condensation to which belongs the source (numbering of DEH09)

^f Classification from DEH09 using color-color and magnitude-color diagrams

^g Classification using the $L_{\lambda \geq 350 \mu\text{m}}/L_{\text{bol}}$ criteria from [Bontemps et al. \(2010a\)](#). If $L_{\lambda \geq 350 \mu\text{m}}/L_{\text{bol}} < 0.01$, the class of the source is at least I

^h Infrared counterparts within a radius of 4'': * stands for IR counterparts seen but not measured. ** stands for source whose counterparts (if any) might be affected or misled by heated filament (not measured)

ⁱ Average volume density computed from the radius at the reference wavelength. > symbol indicates a lower limit for non-resolved source

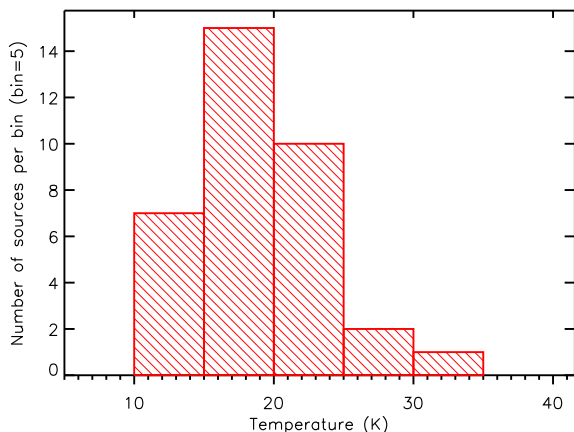


Fig. 11: Envelope temperature distribution for the 35 sources observed towards RCW 120

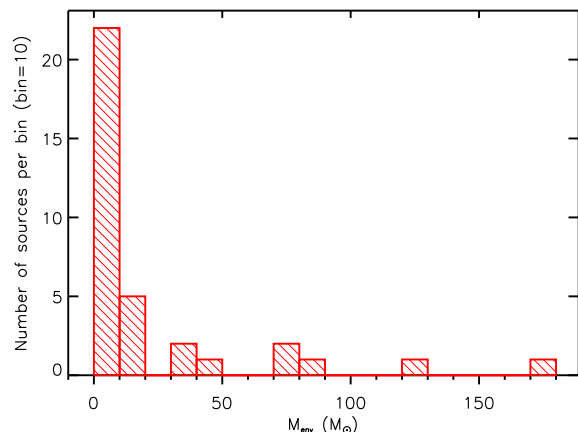


Fig. 12: Histogram of envelope mass for sources observed towards RCW 120

Figure 11 presents the distribution of dust envelope temperature for compact sources observed towards RCW 120. All but three sources (24, 28, 36) have envelope temperature lower than 25 K. As discussed in ZAV07, sources 24 and 28 are observed towards condensation 4. They are classified as Herbig Ae/Be objects and contain a central star of spectral type B4V for source 24 and B7V for source 28. Their extended nature is thought to be the result of local PDR due to radiation of the star but not massive enough to form H II regions which is consistent with the envelope mass derived, $2 M_{\odot}$ and $1 M_{\odot}$ for source 24 and 28, respectively. Source 36 is located in a region of low density and high temperature (23 K).

Figure 12 presents the distribution of envelope mass for sources observed towards RCW 120. Twenty-seven sources have a low mass ($M_{\text{env}} \leq 20 M_{\odot}$) envelope. Sources with envelope mass up to $1 M_{\odot}$ are detected here. From their *Herschel* study of dense cores in NGC 6334, Tigé et al. (2016, submitted) derived an envelope mass limit of $60 M_{\odot}$ (lower limit at which they detect ongoing high-mass star activity) for a core to form a high-mass star. Five sources (2, 9, 10, 39, 94) have envelope mass higher than this limit and four (2, 9, 10, 39) are located in condensation 1. Source 94 is located in condensation 6. The column density towards these condensations is higher than $1.7 \times 10^{22} \text{ cm}^{-2}$. We point out the fact that the high-mass cores represent 15% of the total number of sources in the final sample. Nevertheless, two biases could radically change the result. Firstly, it is possible that the cores are unresolved even at the best *Herschel* resolution ($5''.9$) and represents more than one YSO then decreasing the number of possible high-mass cores. We are confident that source 2 might represent this problematic case. Secondly, our final sample represent reliable sources but is incomplete. According to our selection criteria, the non-selected sources should represent low-mass objects. Consequently, this value of 15% should represent a higher-limit to the number of high-mass cores.

Table 6 summarizes the physical properties of the final sample of sources.

Table 6: Physical properties of the final sample

Physical parameter	T (K)	M_{env} (M_{\odot})	L_{bol} (L_{\odot})	$\langle n_{\text{H}_2} \rangle$ (cm^{-3})
Min	11.2	1	5	2×10^5
Max	34.1	174	1163	1×10^8
Median	19.1	4	30	2×10^6

5.2.4. Properties of the tentative sources

Physical properties of the 87 tentative sources shown in Fig. 7 could not be obtained directly with the SED fitting due to a lack of *Herschel* measurements (see Sect. 4). From the final sample of 35 sources, we fitted the envelope temperature obtained from the SED versus the temperature found at the source location on the temperature map (Fig. 13a). We then used the fitted linear relation to assign a temperature to each of the tentative sources. The mass is computed using the Hildebrand formula (Hildebrand 1983) with one of the *Herschel* fluxes. For the bolometric luminosity, we used the relation between the flux density and the bolometric luminosity ($\log_{10}(F_{\nu}) \propto \log_{10}(L_{\text{bol}})$) using the final sample (Fig. 13b) (Ragan et al. 2012). The relation of Dunham et al. (2008) for embedded protostars is normalized at 1.3 kpc

$$\begin{aligned} \text{Log}_{10}(F_{\nu}^{1.3\text{kpc}}) &= \text{Log}_{10}\left(\left(\frac{0.14}{1.3}\right)^2 F_{\nu}\right) \\ &= 1.06 \text{Log}_{10}(F_{\nu}) - 11.2 \end{aligned} \quad (10)$$

where $F_{\nu}^{1.3\text{kpc}}$ is the flux density at 1.3 kpc and F_{ν} is the flux density of Dunham et al. (2008). This relation is represented in Fig. 13 by the blue-dotted line. Results are given in Appendix B.

5.2.5. Mass of the condensations using the H₂ column density map

Using the H₂ column density map, we derived the mass of each condensation defined by the same area as the one used by DEH09 to compute the mass from APEX 870 μm data. We used the following formula:

$$M = A_{\text{pixel}} \times \mu m_{\text{H}} \times \sum_{ij} N_{\text{H}_2}^{ij} \quad (11)$$

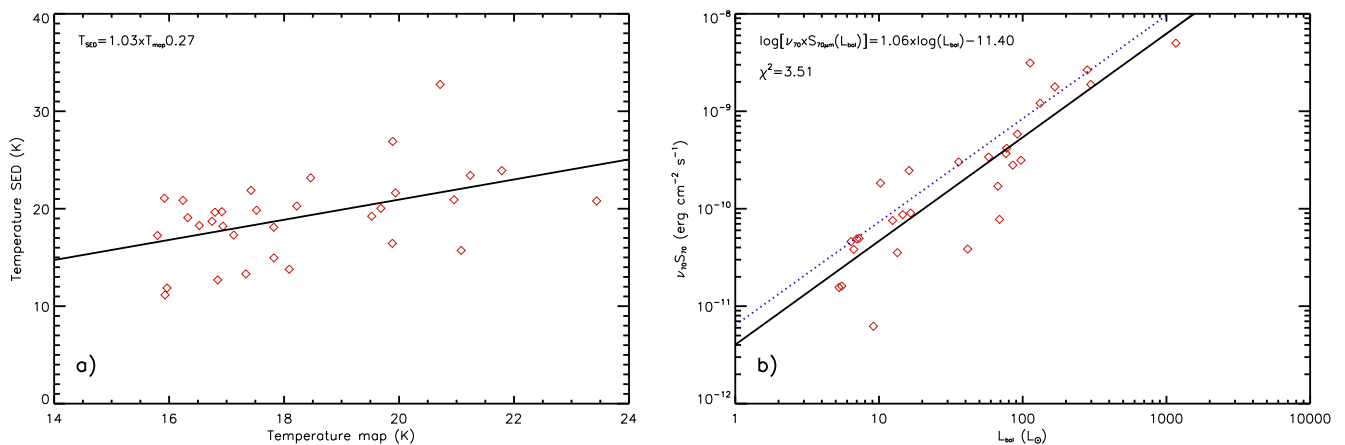


Fig. 13: (a) Temperature given by the SED fitting versus temperature obtained at the source location in the temperature map for the final sample of 35 sources (red diamonds). (b) $\nu_{70\mu\text{m}} \times S_{70\mu\text{m}}$ versus bolometric luminosity for the final sample of 35 sources following Ragan et al. (2012) where the black continuous line represents the fit and the blue dotted one represented the relation from Dunham et al. (2008)

Table 7: Condensations' mass using the low resolution density map (second column) and from DEH09 at 20 K (third column)

Condensation	M_{H_2} (M_{\odot})	$M_{870\mu\text{m}}$ (M_{\odot})
1	2530	800
2	540	192
3	140	63
4	350	88
5	1580	226
6	330	90
7	86	28.5
8	370	38
9	290	42

where A_{pixel} is the area of a pixel in cm^2 , μ is the mean molecular weight (≈ 2.8), m_{H} is the hydrogen atom mass and $N_{\text{H}_2}^{ij}$ is the H_2 column density value at pixels (i,j) . DEH09 computed the mass using the Hildebrand formula with $T=20$ K (and also with $T=30$ K but this value for the condensations is too high compared to the ones derived from the *Herschel* temperature map). The results are given in Table 7. Column 1 gives the condensation number from DEH09. Column 2 gives the condensation's mass derived using the H_2 column density map and Eq. 11, and column 3 the mass derived by DEH09 using the $870 \mu\text{m}$ data, assuming a dust temperature of 20 K.

Compared to DEH09, we obtain higher masses for the condensations. At first sight, the absence of background subtraction could explain this difference but since they are massive, the background only accounts for a small amount of the total pixels value. The main difference between the two results could be explained by the extending emission filtering of the ground-based telescope at $870\mu\text{m}$, leading to an underestimation of the mass (Csengeri et al. 2016). We point out that the condensation mass is critical for star-formation rate and star-formation efficiency estimates that will be further analyzed in a forthcoming paper (Liu et al. submitted).

6. Discussion

6.1. Compact sources' evolutionary stage

As the submillimetric luminosity depends on the envelope mass and the bolometric luminosity on the stellar mass, André et al. (1993) proposed to use the submillimetric to bolometric luminosity ratio as an evolutionary indicator. Bontemps et al. (2010a) used the same kind of criteria to distinguish Class 0 and Class I objects in the Aquila Rift using *Herschel* data but the limits used were different. Class 0 are defined with $L_{\lambda \geq 350\mu\text{m}}/L_{\text{bol}} > 0.03$ while it is higher than 0.01 for Class I. The region between 0.01 and 0.03 contains sources with uncertain classification.

Figure 14 shows the distribution of sources' envelope temperature, color-coded according to their $L_{\lambda \geq 350\mu\text{m}}/L_{\text{bol}}$ value. As expected, there is a relation between the $L_{\lambda \geq 350\mu\text{m}}/L_{\text{bol}}$ value and the envelope temperature of the source. Class I objects (in red) have a higher temperature than Class 0 objects (in green) while the uncertain cases (in blue) are located in between.

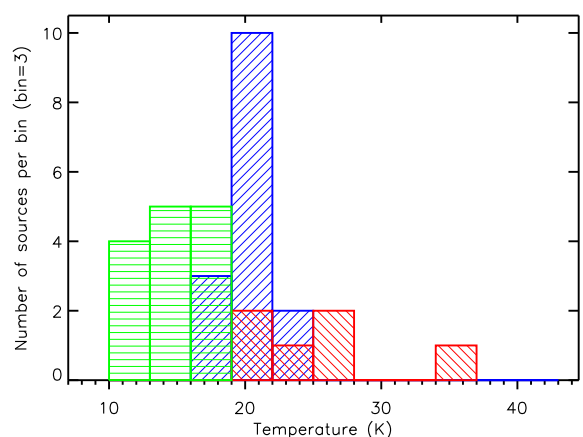


Fig. 14: Histogram of the temperature color-coded according to $L_{\lambda \geq 350\mu\text{m}}/L_{\text{bol}}$ in green for Class 0, red for Class I and blue for uncertain cases

Figure 15 shows the sample of the 35 compact sources on the $L_{\lambda \geq 350 \mu\text{m}}/L_{\text{bol}}$ versus M_{env} diagram coded depending on their location with respect to the PDR. 80% of the sources are located in the Class 0 region with $L_{\lambda \geq 350 \mu\text{m}}/L_{\text{bol}} > 0.01$. If an age gradient was at work in the region, sources towards the PDR would have been under the Class I limit and sources outside the PDR would have been above the Class 0 limit. Depending on the Class 0 limit taken, 1% for André et al. (1993) or 3% for Bontemps et al. (2010a), a weak trend in favor of very young objects out of the PDR can be seen. Towards the PDR, no trend is seen since these sources spread over the entire range of $L_{\lambda \geq 350 \mu\text{m}}/L_{\text{bol}}$ values.

Saraceno et al. (1996) presented the evolution of Class 0 to Class II via spherical accretion by a path in the $L_{\text{bol}}-M_{\text{env}}$ diagram. The unknown mechanism of massive star formation (scaled-up analogue of low-mass star or merging of low-mass stars) and the difficulties of establishing the evolution phase for individual YSOs ($d \geq 1$ kpc, non-resolved clusters) make the construction of an evolutionary scenario for high-mass objects difficult. An attempt has been made by Molinari et al. (2008) to reproduce the $L_{\text{bol}}-M_{\text{env}}$ evolutionary paths for massive objects. From a sample of 42 sources characterized by their [25-12] color value, they classified them as IR-sources if the SED could be fitted with a zero age main sequence (ZAMS) model or MM-sources if a MBB model was used. This difference in the SED translates into a different location in the $L_{\text{bol}}-M_{\text{env}}$ diagram well separated by a line representing IR-sources (see Molinari et al. 2008) practically equivalent to the strip of low-mass Class I objects from Saraceno et al. (1996). Assuming a scaled-up analogue of the low-mass star regime with a turbulent core, a model of time dependent accretion rate (McKee & Tan 2003) with fixed final stellar masses and core surface densities, evolutionary paths in the $L_{\text{bol}}-M_{\text{env}}$ have been computed. The first sequence (indicated in Figs. 16, 17 and 18) represents the accretion phase where the luminosity is dominated by the accelerated accretion and the loss of envelope mass is due to accretion, outflows and possible draining by other YSOs. At the end of the first phase, the star reaches or is close to the ZAMS with a final stellar mass. During the second phase (also indicated in the figures), the envelope mass continues to decrease (the increase of stellar mass by residual accretion is neglected in this model) and the luminosity is now the sum of accretion and stellar luminosity. The final point of the paths corresponds to a loss of 90% of the envelope mass for the four low-mass tracks and to a time of 2.1×10^6 yrs and 2.7×10^6 yrs when the star is optically visible for the two highest-mass tracks. We warn readers that this is a simple model which cannot be used to predict accurately the evolution of YSOs but rather to obtain indication about the evolutionary class of a source.

In Fig. 16, we plot the evolutionary paths for low-mass (Saraceno et al. 1996) and high-mass stars (Molinari et al. 2008) with their corresponding stripes for Class I sources and include our sample. Sources with $M_{\text{env}} > 10 M_{\odot}$ are all located under the Class I stripe and a qualitative analogy with Fig. 9 of Molinari et al. (2008) permits a rough classification of them : sources 1,2,3,5,8,14 are Class I and sources 9,10,39,40,63,94,179 are Class 0. On the contrary, the distribution of sources with $M_{\text{env}} < 10 M_{\odot}$ has a higher dispersion around the Class-I strip, also seen in fig. 9 of Molinari et al. (2008). As in Fig. 15, sources located outside the PDR might tend to be younger but no evidence for a more evolved stage for sources located inside the PDR is seen, as it could have been expected if star formation progresses gradually in the surrounding medium, following the expansion of the ionization front and the leaking of the ionizing radiation.

In Figure 17, the sources are color-coded depending on their location in the condensations. We see a clear trend for the sources' envelope mass and evolutionary stage to be determined by their hosting condensation: sources observed towards condensation 1 have the highest envelope mass and are in low evolutionary stage while sources in condensation 5 are low mass envelope sources, and possibly in a later evolutionary stage. Sources observed towards condensation 4 (pre-existing clump) tend to be evolved and of intermediate envelope mass. Condensation 8 is observed further away from the ionized front and hosts sources in a low-evolutionary stage. Sources 50 and 155 do not belong to any condensation according to DEH09 but are spatially close, outside the PDR and in a similar evolutionary state than the sources in condensation 5. Sources in condensation 2 show a higher dispersion in this diagram compared to the other condensations. The eastern part of condensation 2 contains Class 0-Class I objects of intermediate mass and low-mass objects in the western part. The eastern-part of this condensation seems to be radiation-shielded thanks to the filament in front of sources 3, 8 and 16 while the western-part receives a significant part of the radiation through photons' leaking. This might explain the dispersion of sources' properties observed towards this condensation.

In Figure 18, the sources are color-coded depending on their $L_{\lambda \geq 350 \mu\text{m}}/L_{\text{bol}}$ value. We note that the magenta diamond sources ($L_{\lambda \geq 350 \mu\text{m}}/L_{\text{bol}} < 0.01$) are above the Class I stripe of Saraceno et al. (1996), red square sources ($L_{\lambda \geq 350 \mu\text{m}}/L_{\text{bol}} > 0.03$) are below the Class I stripe of Molinari et al. (2008) and blue triangle sources ($0.03 > L_{\lambda \geq 350 \mu\text{m}}/L_{\text{bol}} > 0.01$) are spread around these stripes. Hence, the two methods give consistent results to derive sources' evolutionary class.

We suggest that the main parameter that controls the star formation and the evolutionary stage of the YSOs is the column density of their hosting condensation. This means that a simple search for YSOs' age gradient around H II region cannot be used as a simple indicator for establishing evidence for triggered star formation.

6.2. Evolutionary stage derived by DEH09

Color-color diagrams using near- and mid-IR data can also be used to infer the class of a source. DEH09 used *Spitzer* GLIMPSE and MIPS GAL colors to discuss the evolutionary stage of YSOs observed towards RCW 120. The results are given in columns 8 and 9 of Table 5. Fig. 19 to Fig. 25 present a zoom of the sources observed from condensation 1 to 8 on the gradient image of the *Herschel* PACS 70 μm emission and the 870 μm emission in contours. All the sources in these figures are detected by *getsources* and identified according to their *getsources* identification number in Table 5 and Table A.1. Final-sample sources, and those identified by DEH09 are indicated in the figures. Hence, non-labelled sources are either not part of the final sample and/or not detected by DEH09. In the following we compare the evolutionary class of sources obtained from mid-IR color-color diagrams (DEH09) with the one obtained in this paper.

Condensation 1 (2530 M_{\odot}) : This is the most massive and densest condensation observed. The classification of Source 9 (40) and 63 (37) do not agree with DEH09. Both objects do not have IR-counterpart in the J, H and K_s and following Fig. 5 of DEH09, they have a $K - [24]$ higher than 10 mag. Hence, they are likely to be in an early evolutionary stage. Source 2 is the massive Class 0 object discussed in Zavagno et al. (2010) (see also DEH09). It is located at the peak of the column density dis-

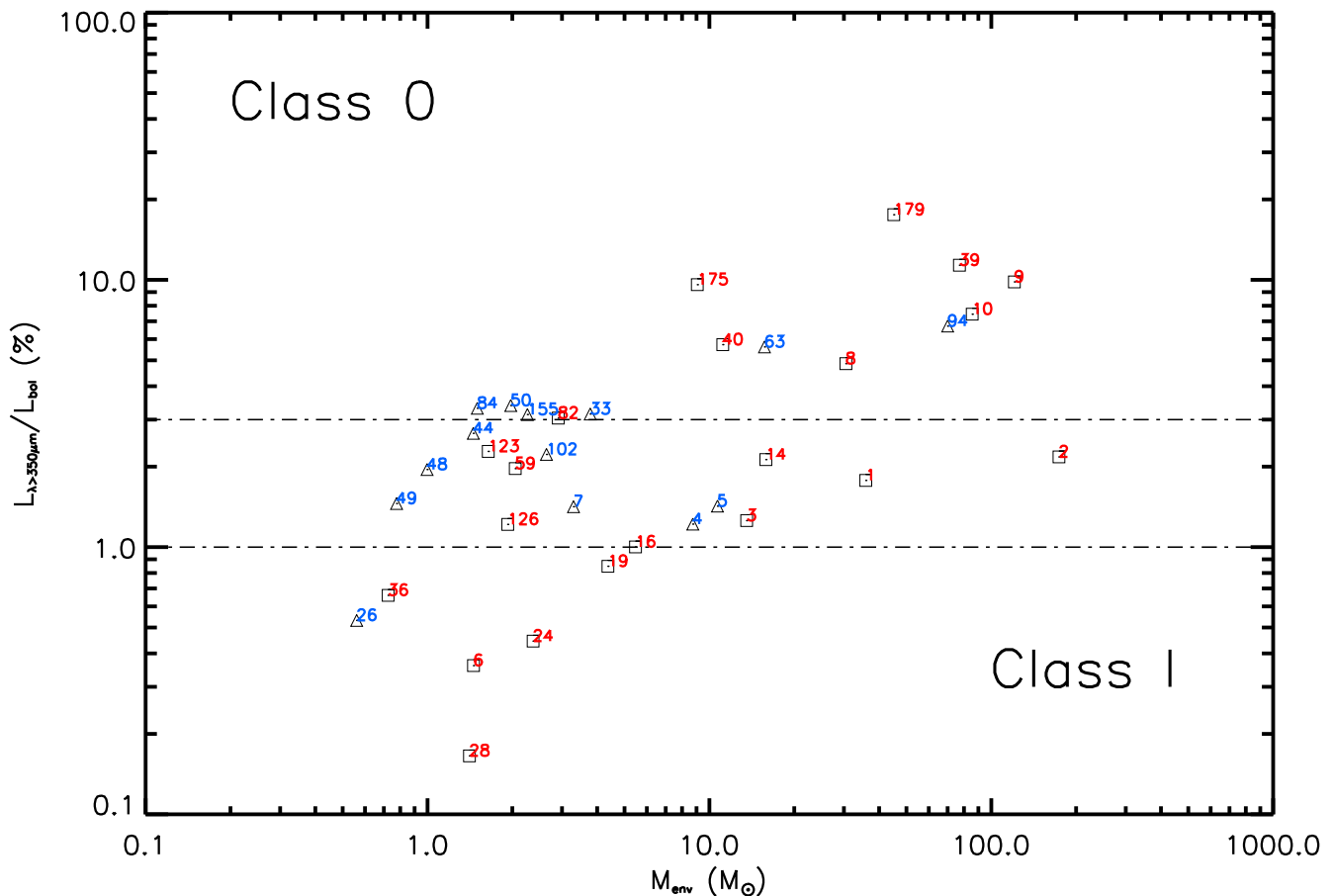


Fig. 15: $L_{\lambda>350\mu\text{m}}/L_{\text{bol}}$ versus M_{env} . The dotted-dashed lines represents the $L_{\lambda>350\mu\text{m}}/L_{\text{bol}}$ limits between Class 0 and Class I from Bontemps et al. (2010a) and sources are color-coded depending on their location: red squares for sources inside the PDR, blue triangles for outside

tribution ($N(H_2) = 4 \times 10^{23} \text{ cm}^{-2}$) and has the highest envelope mass ($M_{\text{env}} = 174 M_{\odot}$) and bolometric luminosity ($L_{\text{bol}} = 1163 L_{\odot}$) of the sample. It is probably a Class 0 source, since no IR-counterpart is detected. Sources 10, 39 and 82 are not detected by DEH09 and are classified as Class 0. This condensation hosts 80% of the massive cores. Because condensation 1 is the densest and most massive in RCW 120, the core formation efficiency (CFE) is expected to be higher compared to the other condensations (Motte et al. 1998; Bontemps et al. 2010b; Liu et al. submitted).

Condensation 2 ($540 M_{\odot}$): Source 3 (50) has been classified as a Class I source by DEH09 in agreement with our classification. Sources 16 and 36 are not discussed by DEH09 maybe because of the high filamentary background around these compact sources. Therefore, no IR-counterpart could be reliably detected and the sources are classified as Class 0-I.

Condensation 4 ($350 M_{\odot}$): Sources 6 (76), 14 (69) and 19 (67) are classified as at least Class I objects and in agreement with DEH09. Source 24 (Object A) and 28 (Object B) are surrounded by local PDR revealed as shells on the gradient $70 \mu\text{m}$ image. Because their IR counterparts are diffuse, no attempt has been made by DEH09 to classify them but are likely Class I or further. ZAV07 suggested that this condensation could be a pre-existing clump engulfed in the ionized region. A subsequent RDI process could have accelerated the collapse which might explain why the objects are in a higher evolutionary stage compared to the other condensations.

Condensation 5 ($1580 M_{\odot}$): This region is highly structured and hosts nine YSOs among the 35 discussed. Among the sources of the final sample and discussed by DEH09, source 33 is the only one whose class does not agree. In the same way as sources 9 and 63 in condensation 1, DEH09 did not measured any near IR-counterpart for this source and its $K - [24]$ value should also be higher than ten. Therefore, this source is also in an early evolutionary stage. Sources 44 and 48 present

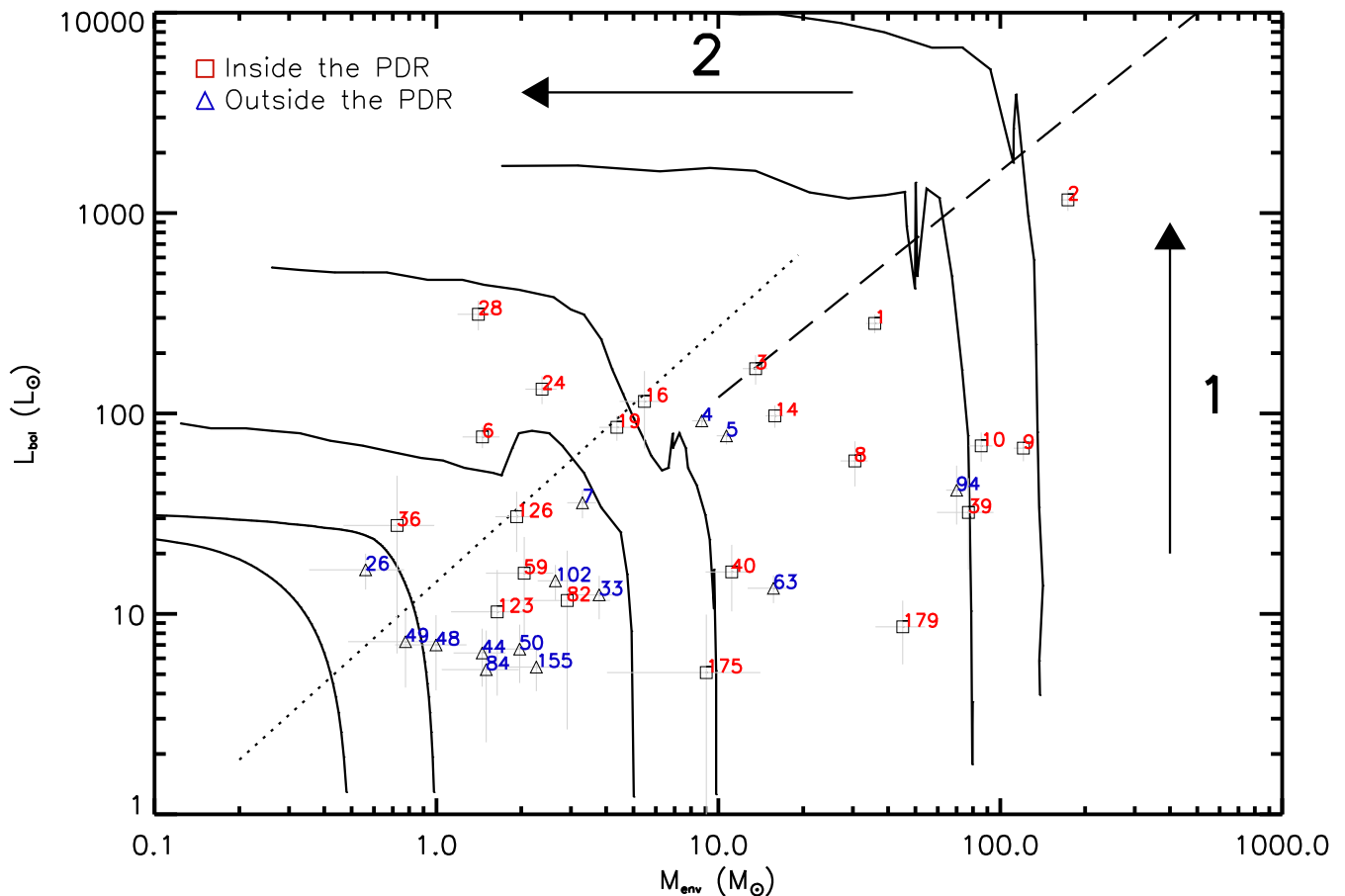


Fig. 16: L_{bol} versus M_{env} . Evolutionary tracks are adapted from Saraceno et al. (1996) and Molinari et al. (2008). Labeled arrows indicate (1) the accretion phase and (2) envelope cleaning phase. Sources are coded as a function of their location with respect to the PDR : red squares sources are for the ones observed towards the PDR and blue triangles for those outside. Error bars for L_{bol} and M_{env} are shown by gray lines

IR-counterparts at all wavelengths except $8\mu\text{m}$ and only at $24\mu\text{m}$ respectively but are too weak ($M_{\text{env}}=1 M_{\odot}$) to be discussed by DEH09. They probably are weak Class I sources. Sources 84 and 123 do not present IR-counterparts and are classified as Class 0.

Condensation 6 ($330 M_{\odot}$) : We identify a massive YSO (source 94) of $M_{\text{env}}=70 M_{\odot}$ with IR-counterparts but classified as Class 0. It is possible that the higher fluxes coming from source 4 contaminates source 94 at long wavelengths hence overestimating the $L_{\lambda \geq 350\mu\text{m}}/L_{\text{bol}}$ value and hence, the classification.

Condensation 8 ($370 M_{\odot}$) : Located south of the ionized region (see Fig. 5b) the zone where the source is embedded, this source was probably formed by the leaking of UV photons passing through the low density medium seen on the high resolution density map (see Fig. 5b) at $(258^{\circ}07', -38^{\circ}52')$. Hence, sources 175 and 179 were probably formed later compared to the sources located in the PDR. This is confirmed by their low-temperature (between 11.2 K and 13.3 K), low evolutionary stage and the absence of IR counterparts.

6.3. Comparison with the Walch et al. (2015) model

Walch et al. (2012, 2013) show that clumpy, shell-like structures like that seen in RCW 120 are probably attributable to pre-existing density structures in the natal molecular cloud. During the expansion of the H II region and the collection of the dense shell, the pre-existing density structures are enhanced and lead to a clumpy distribution within the shell. The masses and locations of the swept-up clumps depend on the fractal density structure of the molecular cloud, through the parameters n and ρ_0 , related to the fractal dimension of the cloud and the density, respectively (Walch et al. 2013, see Sect. 2).

Walch et al. (2015) compared simulations and APEX-LABOCA $870\mu\text{m}$ observations of RCW 120. They performed three-dimensional SPH simulations of H II regions expanding into fractal molecular clouds in order to investigate whether the formation of massive clumps in the swept-up shell necessarily requires the C&C mechanism (Elmegreen & Lada 1977). They show that a distribution of clumps similar to the one seen in RCW 120 can be explained by a non-uniform initial molecular cloud structure, implying that a shell-like configuration of massive clumps does not imply that the C&C mechanism is at work. They find a hybrid form of triggering, which combines elements of C&C mechanism and RDI.

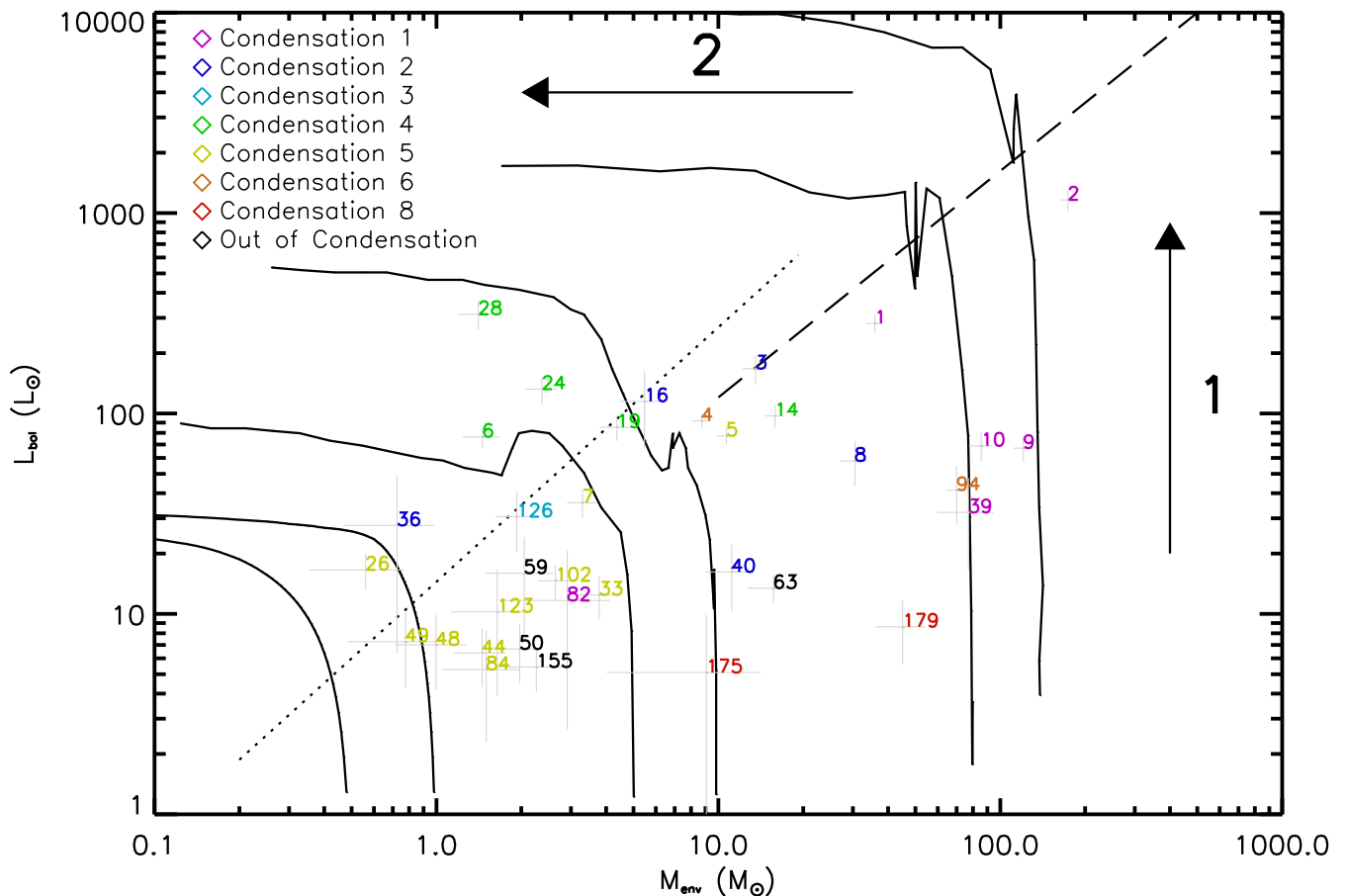


Fig. 17: Same as Fig. 16 but sources are color-coded as a function of their hosting condensation previously identified using the 870 μm and 1.3 mm emission (ZAV07, DEH09). The condensation number refers as the one given in Fig. 5 (left)

We discuss below how the *Herschel* results presented here compare with their findings. The temperature map obtained from *Herschel* images indicates that dust temperatures lower than 30 K, the temperature used by Walch et al. (2015), are observed. This means that the mass they derived for the condensations represents a lower limit. The H_2 column density maps obtained from *Herschel* images show that the observations better correspond with a low value of ρ_0 , where ρ_0 is the scaling constant for the density fluctuations field characterizing the width of the density PDF (Walch et al. 2012, 2013). However pillars are not observed on the northern, lower density part of the ionized region as obtained in their simulations (Walch et al. 2015, fig. 2). This suggests that the numerical treatment adopted better describe higher density regions while lower density regions seem to be better represented by the higher value of ρ_0 .

The distribution of sources observed towards the central part of the ionized region in the simulation is also not observed (Walch et al. 2015, their Fig. 2 right). The distribution of sources in condensations is also not well reproduced by this model, as seen on Fig. 6 and 7. The number of sources they found towards the three main condensations well corresponds with our findings - nine sources towards condensation 1 (their condensation 3), three sources towards condensation 2 (their condensation 1) and six sources towards condensation 4 (their condensation 2). For the two runs, the condensation 3 formed the highest number of high-mass protostars (12.7 M_\odot and 19 M_\odot in average). This is

in agreement with the observations where high-mass cores are found towards our condensation 1. We remind the reader that the mass computed in this paper is the envelope mass while Walch et al. (2015) use the protostars mass. Therefore, it is not surprising that the mass computed in condensation 1 are much higher compared to Walch et al. (2015). Nonetheless, their condensation 2 host protostars of lower masses (9 M_\odot in average) while our corresponding condensation contains low-mass cores. A new modeling of this region using *Herschel* results would help for discussing the star formation history and its propagation in the ambient medium. It would be interesting to discuss the parameters (and mechanisms) that lead to the formation of the high number of high-mass cores observed towards condensation 1.

6.4. Comparison with the model of Torii et al. (2015)

Using MOPRA observations of ^{12}CO , ^{13}CO and C^{18}O in the $J = 1 \rightarrow 0$ transition, Anderson et al. (2015b) did not detect any expansion of the H II region which means that the expansion velocity is either too low to be observed or inexistant. Considering this fact, Torii et al. (2015) explained the formation of the O star and the corresponding ring-like structure following the cloud-cloud collision (CCC) scenario from Habe & Ohta (1992) which can be described in three stages. First, a small and a large clouds are heading towards each other. Secondly, a cavity is created in the large cloud due to the collision with the small cloud.

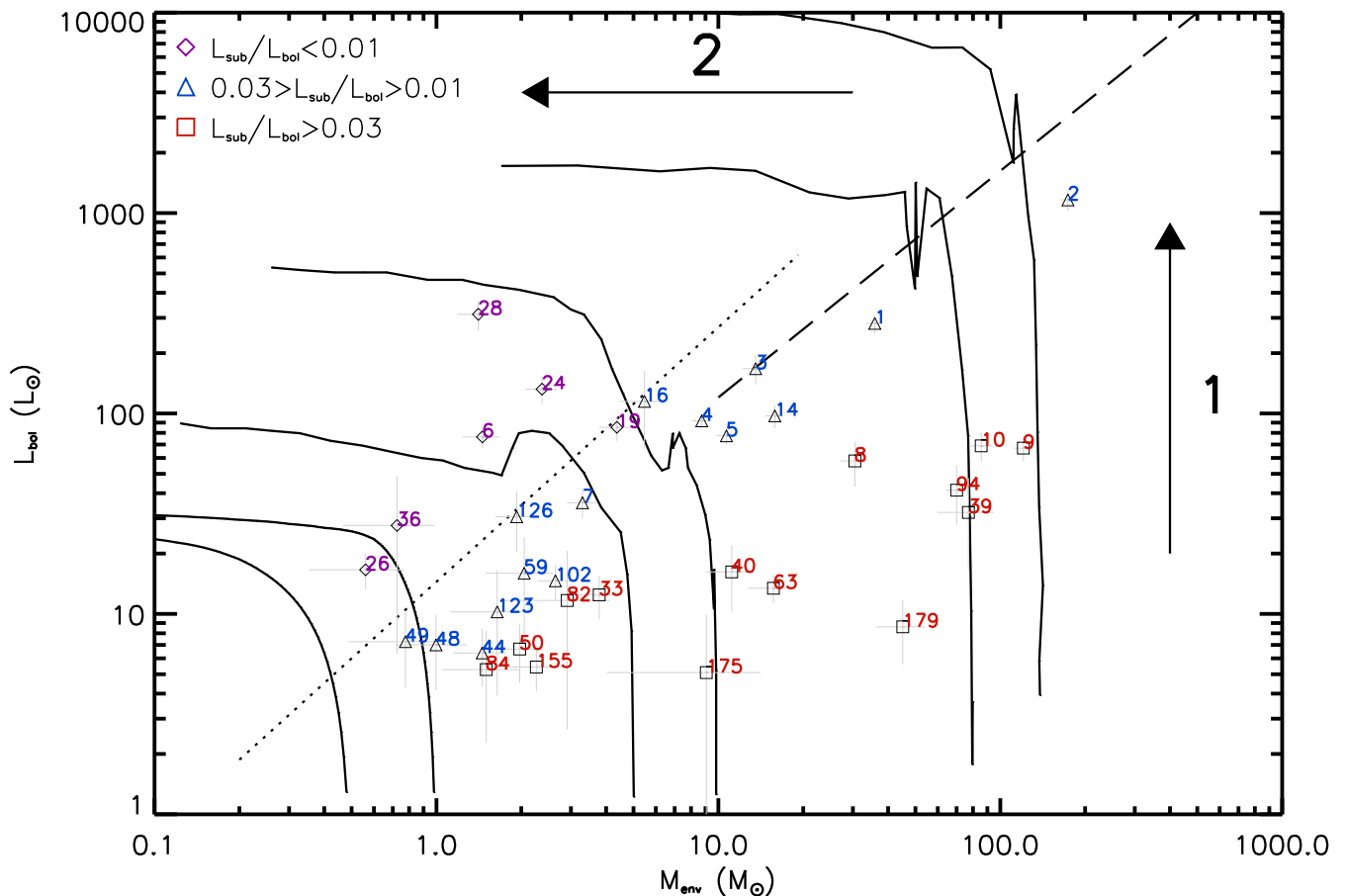


Fig. 18: Same as Fig. 16 but the sources are color-coded as a function of their $L_{\lambda \geq 350 \mu\text{m}}/L_{\text{bol}}$ ratio. Magenta diamonds for Class I objects and red squares for Class 0, while blue-triangle sources are uncertain

The place where the two clumps collided is compressed, leading to massive star formation. Finally, the cavity in the large cloud is filled with the ionizing radiation coming from the recently formed massive star(s). A schematic explanation can be found in Torii et al. (2015) (see their Figs. 12 and 13). In the case of RCW 120, they suggest that the weak leaking of $H\alpha$ emission in the northern part of the ring indicates only the beginning of the erosion by the ionizing radiation. Hence, the triggering which is assumed to take place as a consequence of the C&C mechanism cannot be seen yet. However, after the formation of the ionizing star, a triggering mechanism caused by the compression of the remaining small clump on the large clump is plausible. This could be an alternative explanation which should only affect the formation of YSOs in the southern part of the ring. This study shows that the main driver of the evolutionary stage is the density of the hosting condensation and not the (projected) distance to the ionizing star as expected earlier.

7. Summary and conclusions

We used *Herschel* PACS and SPIRE images, complemented with existing data, to study the star formation observed towards the Galactic ionized region RCW 120.

Zavagno et al. (2010) presented the first results from *Herschel*, however this paper is an in-depth study under the HOBYS recipe which allow us to compare the results between

different regions observed in this key program. Moreover, while the first *Herschel* results were focused on source 2, we produced the first reliable catalog of compact sources using *Herschel* data in this region.

The unprecedented coverage and sensitivity in the far infrared of the *Herschel* data allow us to derive, for the first time, the temperature and H_2 column density map for this region. The temperature ranges from 15 K to 24 K and the column density from $7 \times 10^{21} \text{ cm}^{-2}$ up to $9 \times 10^{23} \text{ cm}^{-2}$. The condensations defined by DEH09 at $870 \mu\text{m}$ corresponds to cold and dense regions where the majority of the sources are detected.

We also derive, for the first time, the envelope mass, envelope dust temperature and bolometric luminosity of compact sources detected there. The temperature ranges from 11.2 K to 34.1 K with a median of 19.1 K, from $1 M_\odot$ to $174 M_\odot$ with a median of $4 M_\odot$ for the envelope mass and from $5 L_\odot$ to $1163 L_\odot$ with a median of $30 L_\odot$. The volume density was computed by assuming a spherical source with the size defined at the reference wavelength ($160 \mu\text{m}$ or $250 \mu\text{m}$) going from $2 \times 10^5 \text{ cm}^{-3}$ to 10^8 cm^{-3} .

We use the physical parameters to discuss the star formation history in this region. We show that most of the compact sources (21 of the 35) are observed towards the PDR.

Thanks to *Herschel* data, we detected 21 sources, mostly in an early evolutionary stage, which were not detected and hence discussed in DEH09.

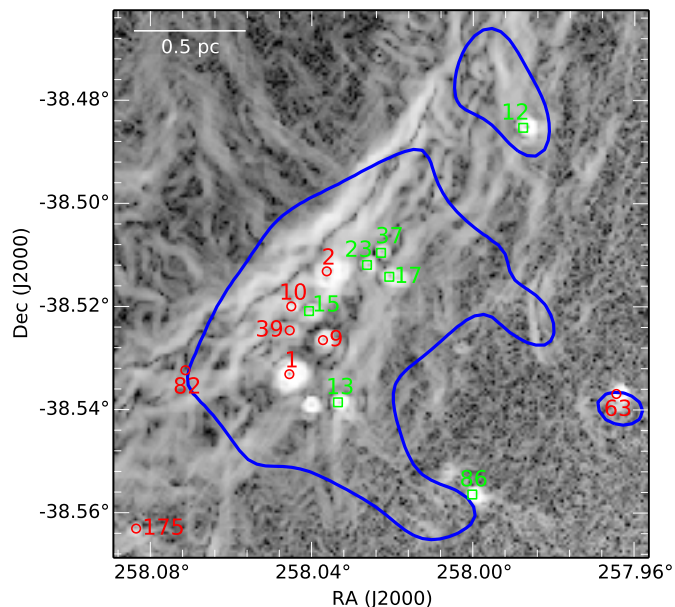


Fig. 19: Condensation 1 and 7: $870\ \mu\text{m}$ emission (countours) superimposed on the gradient image of the *Herschel* PACS $70\ \mu\text{m}$ emission. Sources are identified with their *getsources* identification number. Sources coded with a red circle are those discussed (among the sample of 35 sources). The green square sources are detected but not discussed due to a lack of *Herschel* measurements (see text)

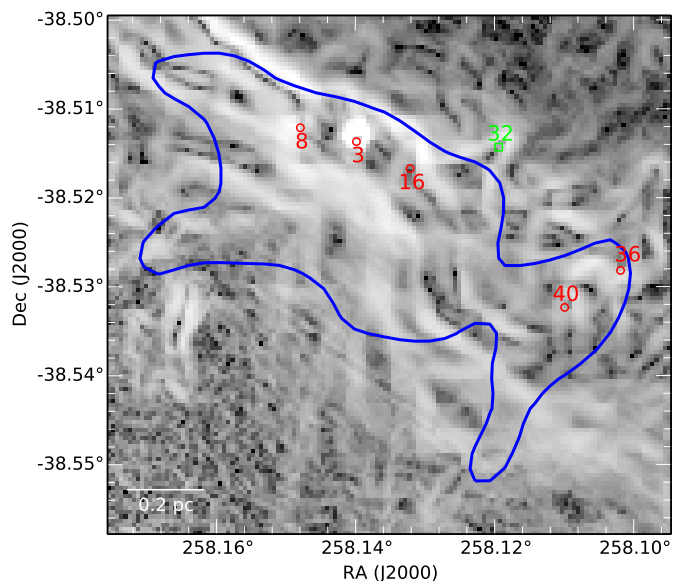


Fig. 20: Condensation 2: same as for Figure 19

Using the $L_{\lambda \geq 350\ \mu\text{m}}/L_{\text{bol}}$ criteria from Bontemps et al. (2010a), we classify the sources between Class 0, intermediate and Class I. We found respectively 15, 16 and 6 sources in this classification.

We find that the projected distance to the ionizing source is not the parameter which controls the evolutionary stage of the sources, contrary to what was expected before, wrongly. In fact, the main driver for this is the density of the condensation where the source is located, whatever its distance to the ionizing sources. Consequently, there is no conflict between possible trig-

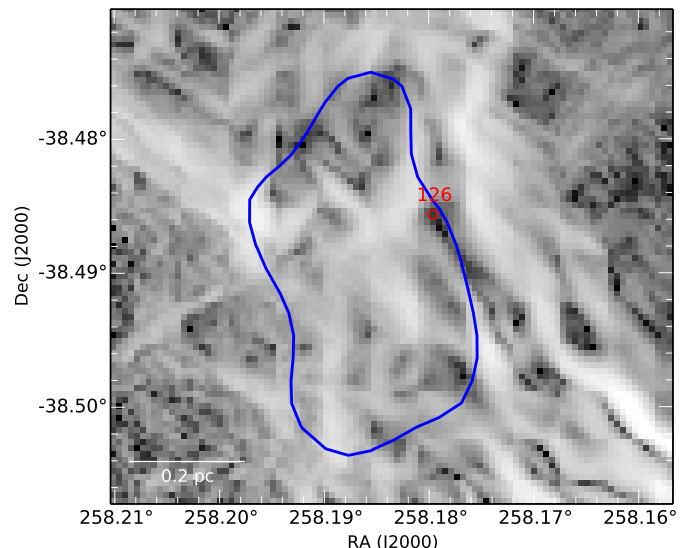


Fig. 21: Condensation 3: same as for Figure 19

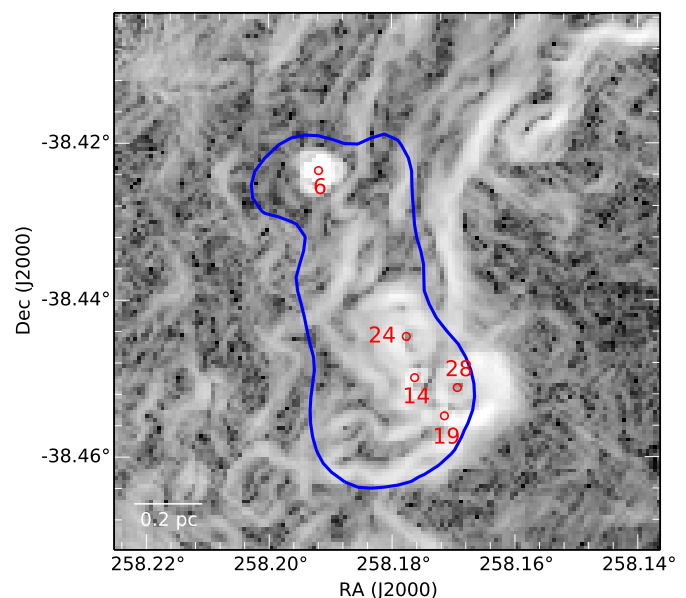


Fig. 22: Condensation 4: same as for Figure 19

gering and projected distance because the density plays a major role in the overall picture. Despite the fact that the southern layer of the region is compressed (Tremblin et al. 2014), *Herschel* data do not allow us to conclude on triggering. High resolution spectroscopic data are needed to determine the structure (possible fragmentation) of the cores and the evolutionary stage of the sources in these cores.

Acknowledgements. We thank the referee for his/her report which helps to improve the quality of the paper. This work is based on observations obtained with *Herschel*-PACS and *Herschel*-SPIRE photometers. PACS has been developed by a consortium of institutes led by MPE (Germany) and including UVIE (Austria); KU Leuven, CSL, IMEC (Belgium); CEA, LAM (France); MPIA (Germany); INAF-IFSI/OAA/OAP/OAT, LENS, SISSA (Italy); IAC (Spain). This development has been supported by the funding agencies BMVIT (Austria), ESA-PRODEX (Belgium), CEA/CNES (France), DLR (Germany), ASI/INAF (Italy), and CICYT/MCYT (Spain). SPIRE has been developed by a consortium of institutes led by Cardiff Univ. (UK) and including: Univ. Lethbridge (Canada); NAOC (China); CEA, LAM (France); IFSI, Univ. Padua (Italy); IAC (Spain); Stockholm Observatory (Sweden); Imperial College London, RAL,

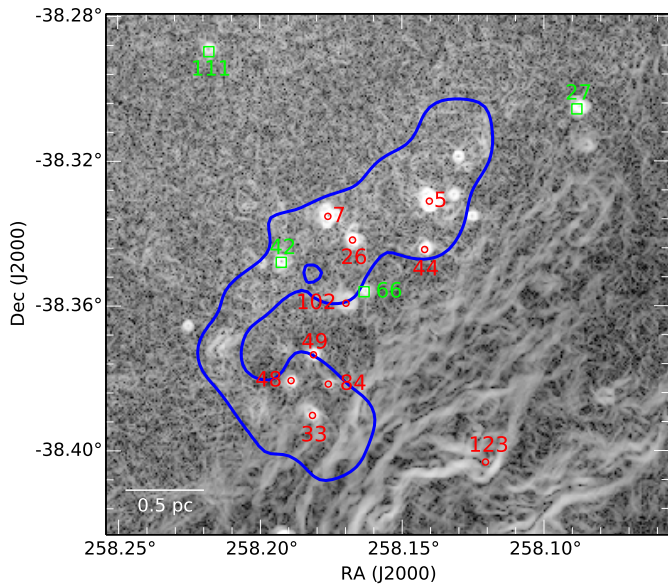


Fig. 23: Condensation 5: same as for Figure 19

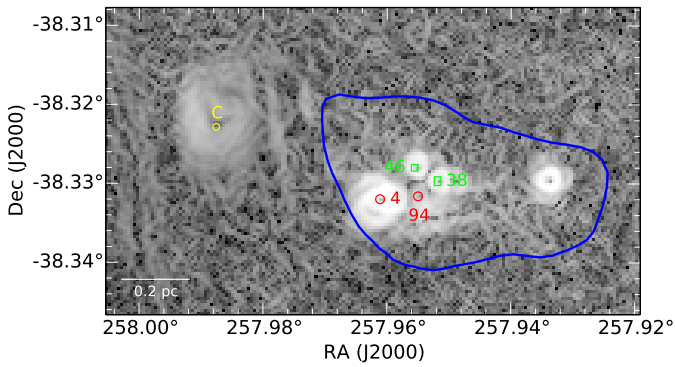


Fig. 24: Condensation 6: same as for Figure 19

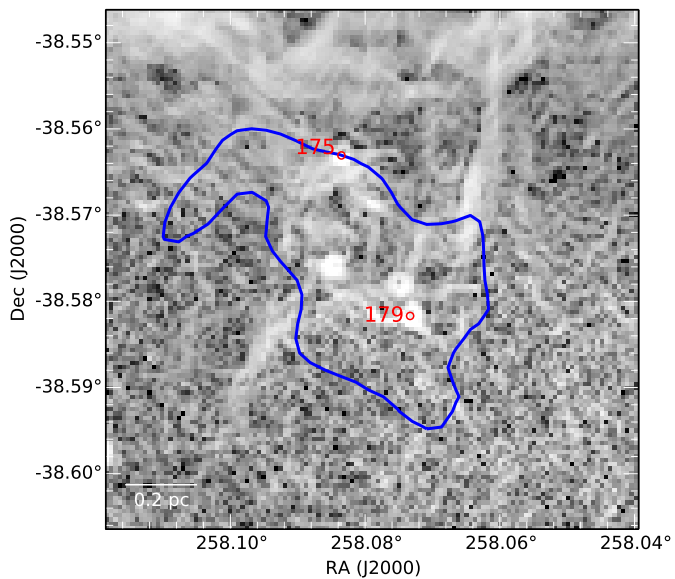


Fig. 25: Condensation 8: same as for Figure 19

UCL-MSSL, UKATC, Univ. Sussex (UK); and Caltech, JPL, NHSC, Univ. Colorado (USA). This development has been supported by national funding agencies: CSA (Canada); NAOC (China); CEA, CNES, CNRS (France); ASI (Italy); MCINN (Spain); SNSB (Sweden); STFC, UKSA (UK); and NASA (USA). This work is based on observations made with the *Spitzer* Space Telescope, which is operated by the Jet Propulsion Laboratory, California Institute of Technology, under contract with NASA. We have made use of the NASA/IPAC Infrared Science Archive to obtain data products from the 2MASS, *Spitzer*-GLIMPSE, and *Spitzer*-MIPSGAL surveys. The Centre National d'Etudes Spatiales (CNES) is deeply acknowledged for the financial support. Part of this work was supported by the ANR (*Agence Nationale pour la Recherche*) project "PROBeS", number ANR-08-BLAN-0241.

References

- Anderson, L. D., Bania, T. M., Balser, D. S., & Rood, R. T. 2011, *ApJS*, 194, 32
- Anderson, L. D., Deharveng, L., Zavagno, A., et al. 2015a, *ApJ*, 800, 101
- Anderson, L. D., Deharveng, L., Zavagno, A., et al. 2015b, *ApJ*, 800, 101
- Anderson, L. D., Zavagno, A., Deharveng, L., et al. 2012, *A&A*, 542, A10
- André, P., Ward-Thompson, D., & Barsony, M. 1993, *ApJ*, 406, 122
- Battersby, C., Bally, J., Ginsburg, A., et al. 2011, *A&A*, 535, A128
- Beckwith, S. V. W., Sargent, A. I., Chini, R. S., & Guesten, R. 1990, *AJ*, 99, 924
- Benjamin, R. A., Churchwell, E., Babler, B. L., et al. 2003, *PASP*, 115, 953
- Bernard, A., Neichel, B., Samal, M. R., et al. 2016, *ArXiv e-prints* [arXiv:1605.07846]
- Bernard, J.-P., Paradis, D., Marshall, D. J., et al. 2010, *A&A*, 518, L88
- Bik, A., Puga, E., Waters, L. B. F. M., et al. 2010, *ApJ*, 713, 883
- Bontemps, S., André, P., Könyves, V., et al. 2010a, *A&A*, 518, L85
- Bontemps, S., Motte, F., Csengeri, T., & Schneider, N. 2010b, *A&A*, 524, A18
- Cappa, C. E., Rubio, M., Romero, G. A., Duronea, N. U., & Firpo, V. 2014, *A&A*, 562, A6
- Carey, S. J., Noriega-Crespo, A., Mizuno, D. R., et al. 2009, *PASP*, 121, 76
- Csengeri, T., Weiss, A., Wyrowski, F., et al. 2016, *A&A*, 585, A104
- Dale, J. E., Haworth, T. J., & Bressert, E. 2015, *MNRAS*, 450, 1199
- Deharveng, L., Schuller, F., Anderson, L. D., et al. 2010, *A&A*, 523, A6
- Deharveng, L., Zavagno, A., Anderson, L. D., et al. 2012, *A&A*, 546, A74
- Deharveng, L., Zavagno, A., Samal, M. R., et al. 2015, *A&A*, 582, A1
- Deharveng, L., Zavagno, A., Schuller, F., et al. 2009, *A&A*, 496, 177
- Dunham, M. M., Crapsi, A., Evans, II, N. J., et al. 2008, *ApJS*, 179, 249
- Dyson, J. E. & Williams, D. A. 1997, *The physics of the interstellar medium*
- Elia, D., Strafella, F., Schneider, N., et al. 2014, *ApJ*, 788, 3
- Ellerbroek, L. E., Bik, A., Kaper, L., et al. 2013, *A&A*, 558, A102
- Elmegreen, B. G. & Lada, C. J. 1977, *ApJ*, 214, 725
- Habe, A. & Ohta, K. 1992, *PASJ*, 44, 203
- Hildebrand, R. H. 1983, *QJRAS*, 24, 267
- Hill, T., André, P., Arzoumanian, D., et al. 2012, *A&A*, 548, L6
- Hill, T., Motte, F., Didelon, P., et al. 2011, *A&A*, 533, A94
- Kendrew, S., Beuther, H., Simpson, R., et al. 2016, *ApJ*, 825, 142
- Kendrew, S., Simpson, R., Bressert, E., et al. 2012, *ApJ*, 755, 71
- Kessel-Deynet, O. & Burkert, A. 2003, *MNRAS*, 338, 545
- Ladeyschikov, D. A., Sobolev, A. M., Parfenov, S. Y., Alexeeva, S. A., & Bieging, J. H. 2015, *MNRAS*, 452, 2306
- Liu, H.-L., Wu, Y., Li, J., et al. 2015, *ApJ*, 798, 30
- Mackey, J., Gvaramadze, V. V., Mohamed, S., & Langer, N. 2015, *A&A*, 573, A10
- Markwardt, C. B. 2009, in *Astronomical Society of the Pacific Conference Series*, Vol. 411, *Astronomical Data Analysis Software and Systems XVIII*, ed. D. A. Bohlender, D. Durand, & P. Dowler, 251
- Martins, F., Pomarès, M., Deharveng, L., Zavagno, A., & Bouret, J. C. 2010, *A&A*, 510, A32
- McKee, C. F. & Tan, J. C. 2003, *ApJ*, 585, 850
- Men'shchikov, A. 2013, *A&A*, 560, A63
- Men'shchikov, A., André, P., Didelon, P., et al. 2012, *A&A*, 542, A81
- Minier, V., Tremblin, P., Hill, T., et al. 2013, *A&A*, 550, A50
- Molinari, S., Pezzuto, S., Cesaroni, R., et al. 2008, *A&A*, 481, 345
- Motte, F., André, P., & Neri, R. 1998, *A&A*, 336, 150
- Motte, F., Zavagno, A., Bontemps, S., et al. 2010, *A&A*, 518, L77
- Nguyen, H., Nguyen Lu'o'ng, Q., Martin, P. G., et al. 2015, *ApJ*, 812, 7
- Nguyen Luong, Q., Motte, F., Hennemann, M., et al. 2011, *A&A*, 535, A76
- Palmeirim, P., André, P., Kirk, J., et al. 2013, *A&A*, 550, A38
- Paradis, D., Paladini, R., Noriega-Crespo, A., et al. 2012, *A&A*, 537, A113
- Parker, Q. A., Phillipps, S., Pierce, M. J., et al. 2005, *MNRAS*, 362, 689
- Pavlyuchenkov, Y. N., Kirsanova, M. S., & Wiebe, D. S. 2013, *Astronomy Reports*, 57, 573
- Planck Collaboration, Aghanim, N., Ashdown, M., et al. 2016, *ArXiv e-prints* [arXiv:1605.09387]
- Ragan, S., Henning, T., Krause, O., et al. 2012, *A&A*, 547, A49
- Rodgers, A. W., Campbell, C. T., & Whiteoak, J. B. 1960, *MNRAS*, 121, 103

- Roussel, H. 2012, Scanamorphos: Maps from scan observations made with bolometer arrays, Astrophysics Source Code Library
- Russeil, D. 2003, A&A, 397, 133
- Samal, M. R., Zavagno, A., Deharveng, L., et al. 2014, A&A, 566, A122
- Saraceno, P., André, P., Ceccarelli, C., Griffin, M., & Molinari, S. 1996, A&A, 309, 827
- Schuller, F., Menten, K. M., Contreras, Y., et al. 2009, A&A, 504, 415
- Simpson, R. J., Povich, M. S., Kendrew, S., et al. 2012, MNRAS, 424, 2442
- Skrutskie, M. F., Cutri, R. M., Stiening, R., et al. 2006, AJ, 131, 1163
- Tapia, M., Persi, P., Roth, M., et al. 2014, MNRAS, 437, 606
- Thompson, M. A., Urquhart, J. S., Moore, T. J. T., & Morgan, L. K. 2012, MNRAS, 421, 408
- Torii, K., Hasegawa, K., Hattori, Y., et al. 2015, ApJ, 806, 7
- Tremblin, P., Anderson, L. D., Didelon, P., et al. 2014a, A&A, 568, A4
- Tremblin, P., Schneider, N., Minier, V., et al. 2014b, A&A, 564, A106
- Walch, S., Whitworth, A. P., Bisbas, T. G., Hubber, D. A., & Wünsch, R. 2015, MNRAS, 452, 2794
- Walch, S., Whitworth, A. P., Bisbas, T. G., Wünsch, R., & Hubber, D. A. 2013, MNRAS, 435, 917
- Walch, S. K., Whitworth, A. P., Bisbas, T., Wünsch, R., & Hubber, D. 2012, MNRAS, 427, 625
- Zavagno, A., Pomarès, M., Deharveng, L., et al. 2007, A&A, 472, 835
- Zavagno, A., Russeil, D., Motte, F., et al. 2010, A&A, 518, L81

Appendix A: Herschel original fluxes for sources detected by getsources (see text)

Table A.1: Identification, position and fluxes for compact sources detected towards RCW 120

Id	Ra	Dec	J	H	Ks	3.60	4.50	5.80	8.00	24.0	70	100	160	250	350	500	
	J2000		mJy														
	Jy																
1	258.04565	-38.53315				2.57	19.12	47.86	69.24	1758.09	62.00	112.80	128.30	83.46	55.01	23.46	
2	258.03625	-38.51318									116.70	625.20	904.20	418.10	240.80	113.90	
3	258.13986	-38.51368			0.65	5.52	24.58	63.16	730.30	1796.11	41.61	57.90	87.31	43.41	13.89	8.16	
4	257.96112	-38.33202			7.25	137.90	315.00	554.40	671.90	2972.66	13.63	21.24	23.04	17.22	12.14	10.65	
5	258.14035	-38.33111		7.41	55.92	393.80	558.15	855.70	951.10	1896.43	9.75	12.01	15.21	17.30	12.45	7.75	
6	258.19193	-38.42351		3.53	31.21	255.00	495.85	819.60	1048.00	2138.66	8.61	12.58	13.03	4.69	3.46	3.52	
7	258.17612	-38.33530				0.56	3.50	2.79		134.73	7.05	14.66	15.45	10.45	7.79	4.45	
8	258.14792	-38.51212									7.92	21.46	56.61	36.86	25.03	11.53	
9	258.03720	-38.52652				2.56	3.01	7.56	8.55	113.64	3.98	12.02	15.76	87.22	55.12	19.56	
10	258.04517	-38.51953					1.35				1.81	11.17	46.55	73.89	28.84	18.83	
14	258.17627	-38.44988	1.38	4.08	8.14	13.15	22.63	35.54	25.73	203.01	7.34	39.30	58.34	33.07	17.25	11.28	
16	258.13214	-38.51672									73.06	93.17	74.14	18.33	4.65	2.76	
19	258.17145	-38.45472	9.76	42.18	104.90	216.90	277.90	356.50	384.40	1176.02	6.54	21.61	33.05	11.79	4.20	0.18	
24	258.17780	-38.44460						0.00	0.00	0.00	28.23	49.36	33.71	11.55	10.73	0.51	
26	258.16742	-38.34184	3.25	9.57	19.89	48.65	87.12	145.60	225.70	505.54	2.11	2.63	2.67	3.08	3.40	3.15	
28	258.16949	-38.45095	0.00	0.00	0.00	0.00	0.00	0.00	0.00	0.00	44.00	89.36	56.69	8.75	2.05	0.10	
33	258.18164	-38.39026			7.08	3.05	8.34	7.57	9.08	118.37	1.77	4.11	7.59	6.85	4.33	2.92	
36	258.10190	-38.52818									8.15	15.50	11.37	5.40	0.27		
39	258.04541	-38.52476		2.53	1.65	3.89	6.13	7.91	33.18		0.59	2.25	0.90	45.98	14.59	7.37	
40	258.10992	-38.53234									5.76	5.94	10.25	10.82	8.47	6.09	
44	258.14203	-38.34447	1.34	2.13	2.73	0.98	3.01	2.64		1.93	1.07	2.44	3.93	3.92	2.36		
48	258.18912	-38.38067								10.53	1.15	2.87	4.89	2.34	2.05	0.01	
49	258.18124	-38.37353			2.58	5.59	11.20	22.07	27.38	137.68	1.16	2.18	3.89	1.47	0.06	1.23	
50	257.95599	-38.40344									0.89	3.04	5.73	3.33	2.45	2.28	
59	258.08347	-38.53136									2.89	8.75	11.01	7.26	0.07	0.62	
63	257.96445	-38.53691								438.16	0.83	1.02	2.45	3.16	4.36	4.96	
82	258.07132	-38.53237									1.44	5.56	8.89	6.99	0.10		
84	258.17609	-38.38145									0.36	2.38	5.17	2.38	0.78		
94	257.95505	-38.33182			2.54	7.99	15.94	20.05	21.25	2477.74	0.90	2.14	5.75	29.01	21.82	1.04	
102	258.16974	-38.35928		4.11	12.21	28.97	27.71	27.61	18.23	6.51	2.03	5.31	8.22	4.74	4.10	2.86	
123	258.12061	-38.40319									4.28	8.29	7.94	4.45	1.97	1.60	
126	258.17963	-38.48564									6.47	17.84	17.31	9.02	0.20	2.36	
155	257.95459	-38.40161	0.81	1.45	2.49	13.60	21.54	32.08	46.89	163.98	0.38	0.75	2.00	2.15	2.17	1.84	
175	258.08353	-38.56308	0.52	1.53	2.13	2.39	3.06	2.60	1.06	9.11	0.35	0.75	4.57	4.49	5.64	1.20	
179	258.07333	-38.58170									0.15	0.79	3.44	4.52	11.27	7.49	
11	258.04062	-38.53902									3.04	6.87	7.30	9.03		15.48	
12	257.98761	-38.48531								159.78	4.14	8.02	9.48	9.82	6.69	8.00	
13	258.03348	-38.53858								483.24	3.82	5.93	9.21	30.84	50.55		
15	258.04065	-38.52089			2.01	19.71	33.76	42.35	19.57		2.56				10.78		
17	258.02078	-38.51423								69.07	3.44	9.61		171.00	67.35		
20	257.93423	-38.32965									1.58	2.52	3.35				
23	258.02631	-38.51194			1.67	1.36	4.90	6.91			1.49	3.67					
27	258.08841	-38.30564									2.25	1.17					

Table A.1: continued.

Id	Ra	Dec	J	H	K	3.60	4.50	5.80	8.00	24.0	70	100	160	250	350	500
			mJy													
			Jy													
32	258.11938	-38.51431				28.17	37.51	54.58	49.70		2.71	4.43	1.13			
34	258.29898	-38.28543				1.04	1.01		5.51	408.27	1.56	0.96				
37	258.02283	-38.50959					3.74	7.20	12.20	238.86	0.94					35.88
38	257.95184	-38.32969				1.72	4.44	5.37	2.84		1.47	2.27	4.52	4.06	8.59	12.71
42	258.19254	-38.34798				0.41	1.35			53.28	1.29	1.40	2.15			
46	257.95554	-38.32800				7.47	22.37	39.95	37.70	134.74	1.04	2.08	2.65			
52	258.09766	-38.51765				3.54		13.45	32.97		3.11	5.88	6.99			
58	258.04913	-38.52470				4.59	3.01	26.98	84.79		1.61	1.73	4.06	40.04	20.09	14.33
66	258.16336	-38.35612			2.62	13.40	26.86	38.75	50.58	194.14	0.77	1.37	1.76			
78	258.09763	-38.52643									0.55	1.15	2.17			
81	258.13211	-38.32971				1.06	2.52	2.68	1.42	17.74	0.44	0.64	0.92			
85	257.94284	-38.23342				1.70	1.16	3.35	11.08	29.17	0.64	0.92	0.60			
86	258.00015	-38.55644								62.96	0.60	0.72	2.20			
87	258.12576	-38.33563				1.00	2.54	3.81	3.74	23.83	0.39	0.85	2.40			
91	257.91385	-38.45134		0.98	4.75	21.70	33.52	37.45	43.50	139.88	0.40	0.96	2.40			
95	258.13080	-38.31924									2.63	2.45	3.44	6.59	6.36	
100	258.26227	-38.35157	17.98	23.16	22.80	12.01		6.78	9.32		1.13	2.08				
103	258.17090	-38.50493									2.60	3.42				
106	258.12173	-38.53703				2.54	2.06			3016.04	0.54	0.30	2.44			
111	258.21793	-38.28977									0.86	1.58				
112	258.29178	-38.46433	0.56	2.17	3.01	4.45	5.42	3.08	5.30		0.47	0.56				
115	258.26550	-38.33118	10.06	18.53	23.59	16.53	10.79	8.72	4.28	15.13	2.17	2.10				
116	258.09653	-38.54058									1.90	3.15				
134	258.19498	-38.48449									0.27	0.50				
135	258.22525	-38.36578									0.29	0.37				
137	257.99088	-38.28571				4.27	13.27	24.62	27.92	27.79	0.84	1.48				
142	258.12906	-38.58107				1.69	2.43	0.99		16.42	1.02	0.88				
145	258.09253	-38.52492				0.88	0.68				0.22	1.36	2.00			9.32
150	258.08490	-38.57631				0.25	0.45				0.35	0.37				
151	258.00430	-38.47361									3.19	5.83	6.89			
152	258.09113	-38.43760										3.50				
157	258.14062	-38.40404									7.42	7.64				
158	257.98721	-38.32267	13.25	16.38	14.59	8.56	8.62				0.82	1.71				
160	258.17786	-38.50867			1.19	1.75	1.26				0.26	0.25				
167	258.30264	-38.51905				0.78	0.45			17.07	20.20	10.82				
172	258.08502	-38.49975	9.06	8.68	6.64	3.67	2.63	1.54			0.61	0.86				
173	258.17233	-38.43617	0.46	8.63	29.94	41.70	27.58	27.66			0.37	0.37				
180	258.00781	-38.49869	0.42	1.94	3.75	4.78	2.77	8.93			1.77	2.78	3.10			
183	258.06735	-38.40066								1533.81	0.22	0.15				
184	258.30685	-38.27173									1.31	1.25				
185	258.10931	-38.53597		1.62	3.74	6.87	5.38				0.27	0.69				
187	258.09045	-38.51449				1.06	0.68									
189	258.18784	-38.45626														

Table A.1: continued.

Id	Ra	Dec	J	H	K	3.60	4.50	5.80	8.00	24.0	70	100	160	250	350	500
	J2000		mJy													
190	257.98822	-38.42171		5.86	66.73			1191.00	1186.00	865.34	0.39	0.24				
200	257.86819	-38.36474	5.91	76.97	290.20			1286.00	1464.00	1158.68	0.23					
202	258.01770	-38.35570									0.20	0.39				
209	258.08630	-38.31583	191.50	380.80	377.00	218.90		93.74	59.72		0.97	0.61				
210	258.11935	-38.59785				0.42	0.78				0.29	0.30				
214	258.00909	-38.41885		0.97	1.36	2.27	1.99	3.58			0.75	0.77				
220	258.09015	-38.42498			1.66	3.13	2.23				0.81	1.37				
222	258.16699	-38.33837										0.68				
225	258.07635	-38.51399										1.95				
231	258.12537	-38.39469									0.49	0.84				
234	258.05734	-38.54539									0.53	0.50				
235	258.08182	-38.33235									0.91	2.63				
241	258.16605	-38.51577									0.82	0.98				
243	258.01715	-38.46565	1.63	2.09	1.68	1.04	0.58				0.45	1.13	1.29			
244	258.07840	-38.38462	3.06	3.33	2.30	1.26	0.78				0.75	1.61				
245	258.10086	-38.35387				0.70	0.59				0.84	1.30	1.70			
248	258.22702	-38.48562				12.46	9.64	8.35			0.87					
253	258.05783	-38.54014		1.64	3.84	3.85	2.85	3.94			0.28					
259	258.13406	-38.38127		1.85	3.87	4.80	3.32	3.68			0.36					
260	258.19949	-38.34837				0.26	0.50				0.14					
262	257.97363	-38.49245				1.00	1.01				0.71		4.51			
265	258.18042	-38.52432				0.79	0.97				0.99					
267	258.13535	-38.46489	4.42	87.16	395.90			1853.00	1500.00	1070.69	0.30					
268	258.11862	-38.26870		0.79	1.11	1.10	0.85				0.79	1.23				
271	258.00577	-38.49241									0.25					
274	258.12790	-38.32248	3.68	3.32	2.37	2.06	4.21	5.22	1.67			0.58				
277	258.22003	-38.46579				1.48	1.31				0.23					
279	258.11310	-38.36686				1.73	1.30				0.20					
282	258.19473	-38.47963			2.54	4.57	3.42	6.82			0.24					
292	258.07513	-38.57813				2.80	7.31	10.89	15.84	63.85	0.23					
295	258.05261	-38.54072									0.33					
300	258.09039	-38.55998	19.48	16.87	11.69	7.03	6.00	6.22	3.18	34.85	0.23					
305	258.18768	-38.42732				1.14	1.17				0.30					
307	258.05716	-38.39042		0.82	1.78	2.55	2.07				0.23					
308	257.87827	-38.31401	2.00	8.39	12.29	9.13	6.45	5.01	4.21	4.74	0.11					
329	258.20914	-38.41260										7.00				

Appendix B: Properties of tentative sources

Table B.1: Tentative-source properties

Id	T K	M_{env} M_{\odot}	L_{bol} L_{\odot}	IR counterpart
11	17.2	11.4	25.3	No
12	18.9	9.1	33.5	Yes
13	16.7	16.6	31.2	Yes
15	17.8	186.9	21.5	Yes
17	17.0	94.6	28.3	No
20	16.5	6.6	13.9	Yes
23	17.6	26.2	13.1	Yes
27	17.9	7.3	19.1	No
32	22.3	0.5	22.7	Yes
34	18.7	4.3	13.7	Yes
37	17.8	69.6	8.5	Yes
38	15.8	11.2	13	Yes
42	16.1	4.8	11.5	Yes
46	16.2	5.7	9.4	Yes
52	23.2	2.7	25.8	Yes
58	18.1	98.9	14.1	Yes
66	16.6	7.5	7.1	Yes
78	22.9	1.9	12.1	No
81	15.9	5.1	5.3	Yes
85	19.9	1.8	4.2	Yes
86	16.9	9.3	6	Yes
87	16.5	8.9	5.7	Yes
91	17.6	3.0	3.8	Yes
95	15.7	6.1	3.9	No
100	18.1	14.0	22.1	Yes
103	20.6	4.5	10.2	No
106	20.9	6.8	21.8	Yes
111	18.6	1.4	5.1	Yes
112	17.9	3.1	7.9	Yes
115	18.1	3.3	4.6	Yes
116	22.4	2.6	18.5	No
134	19.4	10.9	16.4	No
135	16.8	5.3	2.7	Yes
137	16.6	4.3	2.9	Yes
142	17.4	11.9	7.8	Yes
145	23.5	0.8	9.2	No
150	16.1	4.4	2.3	Yes
151	21.1	0.7	3.5	No
152	20.1	5.0	26.4	No
157	20.4	8.2	0.2	No
158	18.9	31.7	57.3	Yes
160	19.8	5.1	7.6	Yes
167	18.1	1.4	2.6	Yes
172	23.1	11.1	144.1	Yes
173	20.0	2.4	5.8	Yes
180	20.6	5.5	3.7	Yes
183	20.1	2.3	15.4	No
184	18.7	0.7	2.2	Yes
185	21.1	3.5	0.2	Yes
187	23.4	1.2	11.6	Yes
189	19.1	2.7	2.8	No
190	19.5	0.8	3.8	Yes
200	19.8	5.2	2.4	Yes
202	18.4	2.0	2.1	No
209	18.5	3.0	8.8	Yes
210	17.7	2.1	2.9	Yes

Table B.1: continued.

Id	T K	M_{env} M_{\odot}	L_{bol} L_{\odot}	IR counterpart
214	21.4	1.3	7	Yes
220	20.3	3.4	7.5	Yes
222	15.9	11.6	0.2	No
225	23.0	2.1	0.2	No
231	19.4	2.8	4.7	No
234	19.5	1.6	5.1	No
235	19.0	10.4	8.3	No
241	19.0	3.8	7.6	No
243	21.0	0.8	4.4	Yes
244	19.6	5.1	6.9	Yes
245	20.1	1.2	7.8	Yes
248	18.4	43.3	8	Yes
253	19.6	7.0	2.8	Yes
259	21.0	1.2	3.5	Yes
260	16.1	5.9	1.5	Yes
262	18.1	5.4	6.6	Yes
265	18.0	8.6	9	Yes
267	20.5	4.7	3	Yes
268	18.8	5.4	7.3	Yes
271	21.6	2.4	2.6	No
274	15.9	9.9	0.2	Yes
277	19.0	3.7	2.3	Yes
279	20.4	1.2	2.1	Yes
282	19.8	1.6	2.4	Yes
292	16.1	57.3	2.3	Yes
295	18.6	14.7	3.3	No
300	18.2	13.1	2.3	Yes
305	18.6	1.6	3	Yes
307	19.8	1.0	2.3	Yes
308	19.6	0.9	1.2	Yes
329	18.5	33.7	0.2	No

Appendix C: Image of the sources

In this section, we present the three first sources of the final sample on the 2MASS, *Spitzer* GLIMPSE and MIPS GAL, *Herschel* and density maps (low and high resolution) together with the result of their SED fitting. The maps ($1' \times 1'$ for IR maps and $2' \times 2'$ for *Herschel* maps) are centered on the coordinates given by *getsources* with the corresponding wavelength written in the upper-left part of the image.

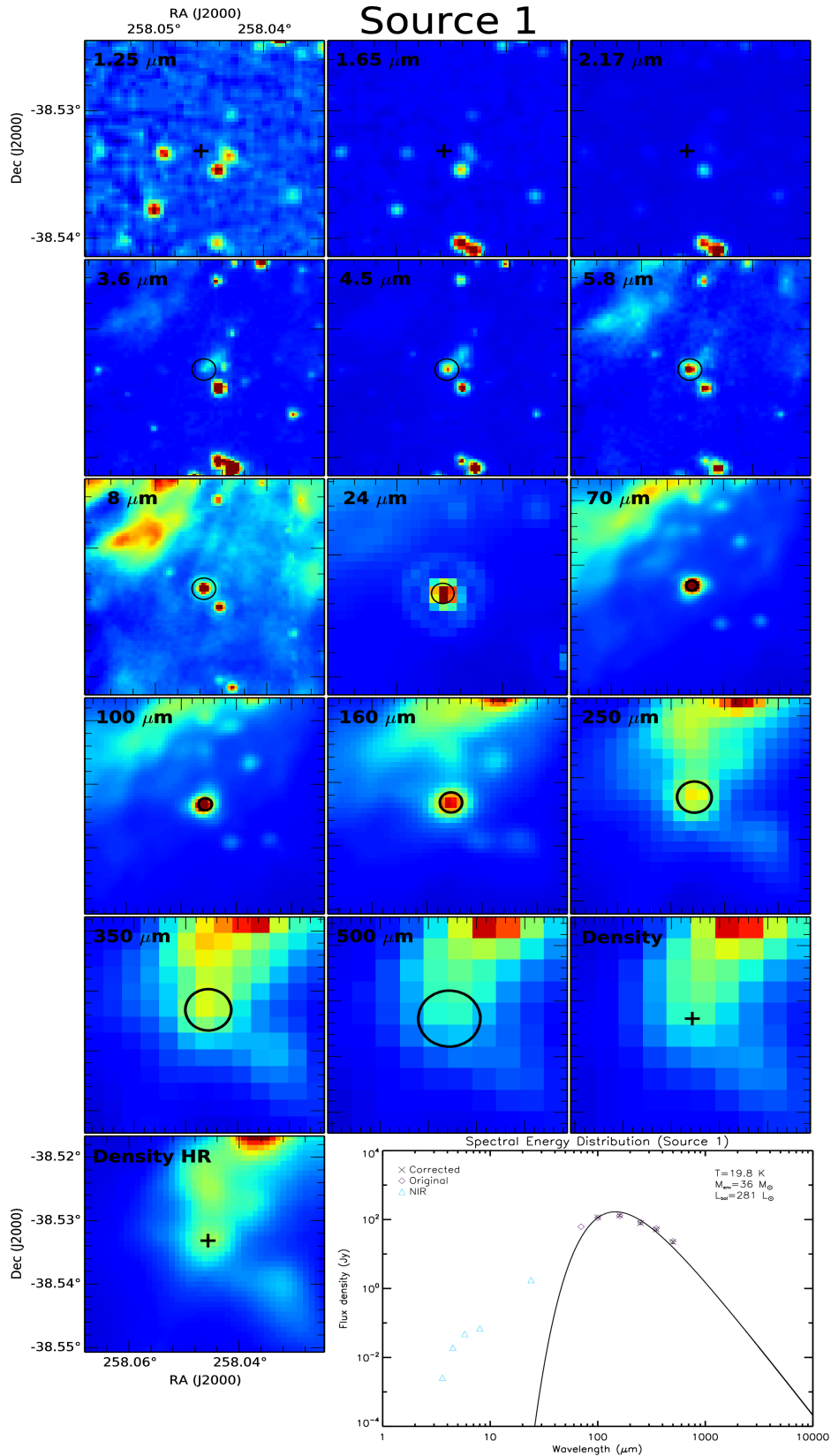


Fig. C.1: 2MASS, GLIMPSE, MIPS GAL, *Herschel*, low-resolution and high-resolution images of source 1. If a counterpart is seen in the infrared catalogs, a black circle of $4''$ radius is shown to indicate the location of this counterpart otherwise, the center (position of the source given by *getsources*) is indicated by a cross. For *Herschel* images, the ellipses shown are the *getsources* parameters, A_{FWHM} and B_{FWHM} . For the representation of the SED fitting, the original fluxes are represented by a magenta diamond, the corrected fluxes (flux scaling + color correction) at the wavelength used for the fitting are represented by a black cross, and the blue triangles represent the IR counterparts, if any. The identification number of the source is given in the title of the SED.

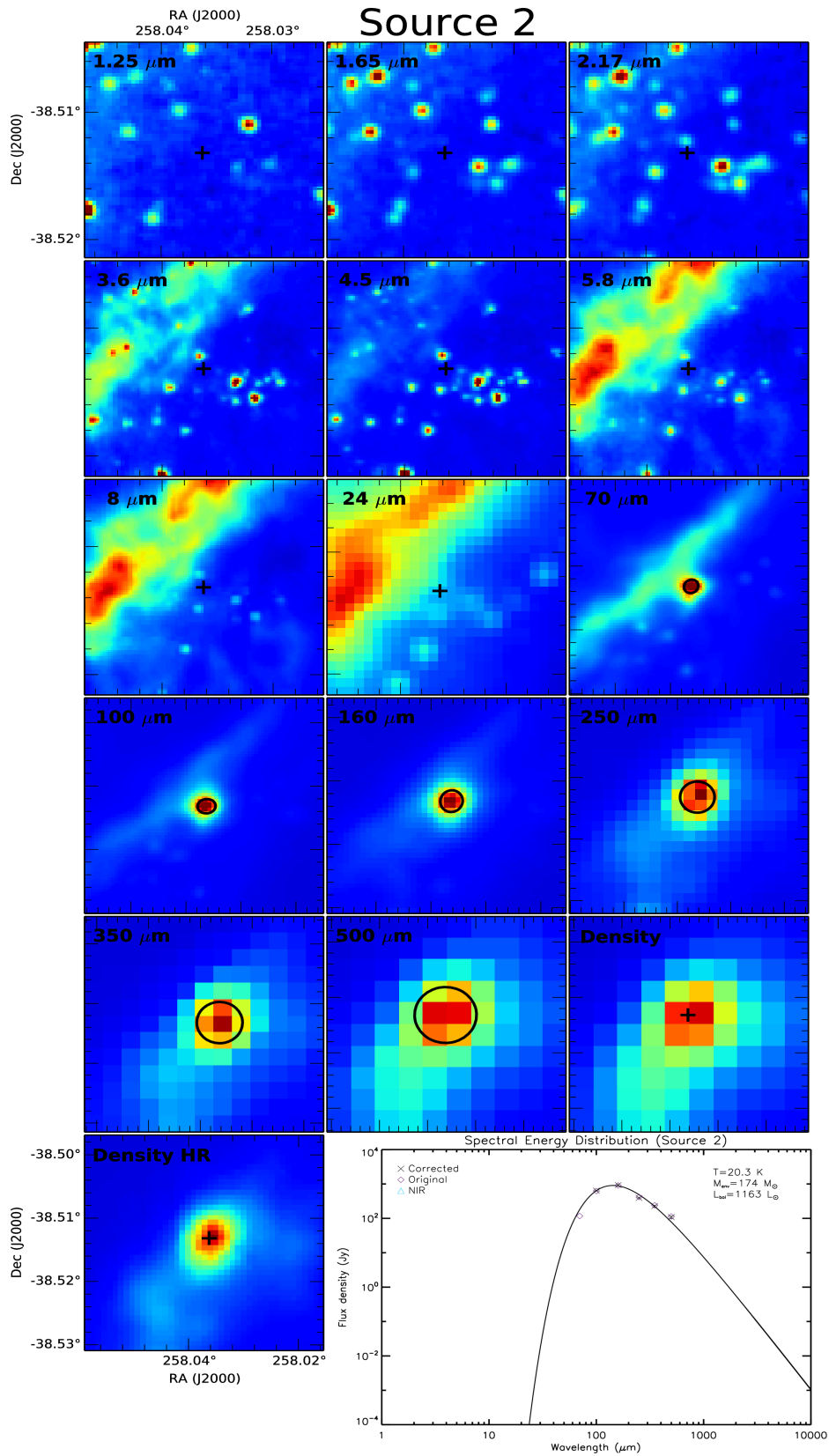


Fig. C.2: Same as Fig. C.1 for source 2

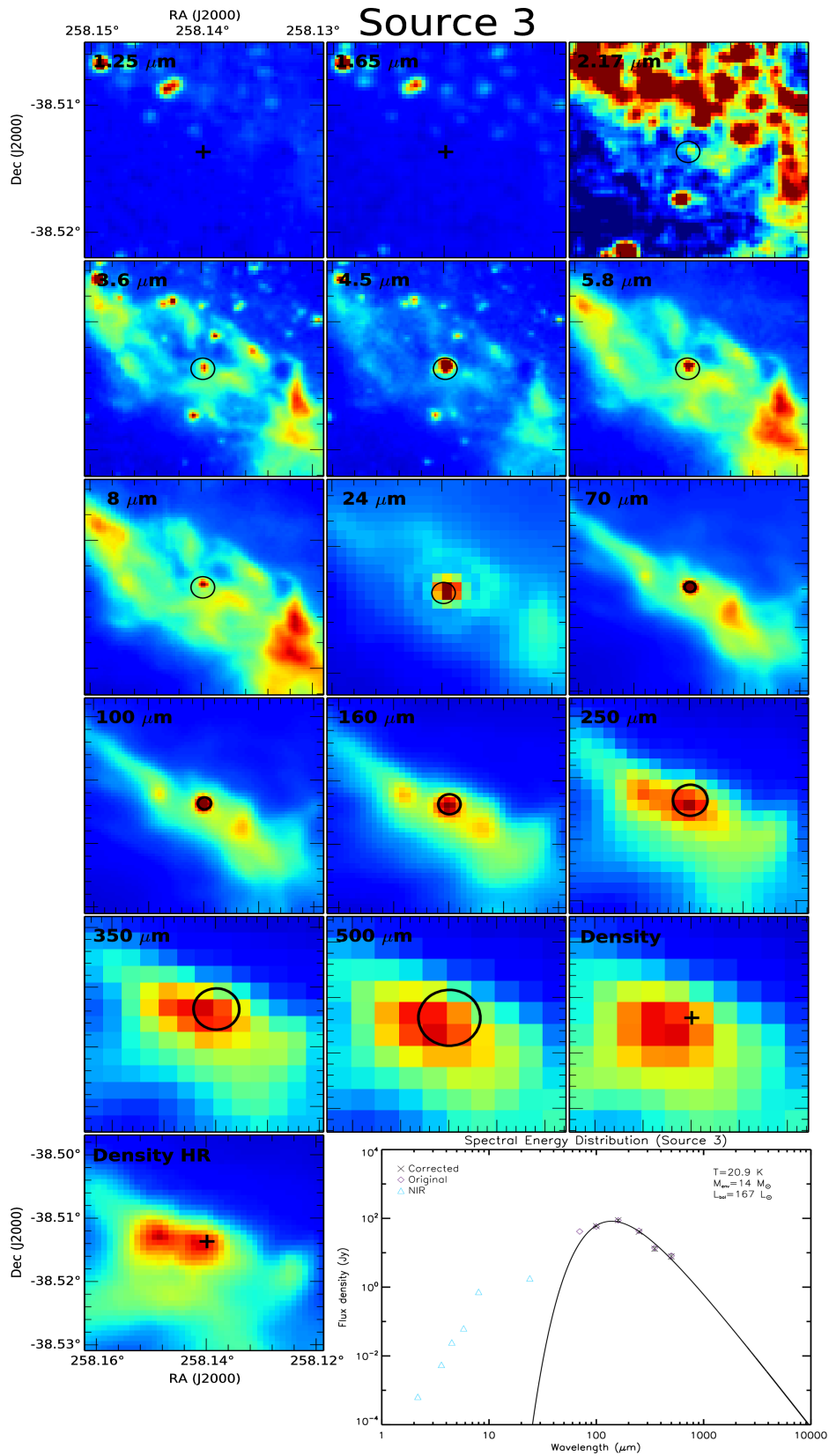


Fig. C.3: Same as Fig. C.1 for source 3